RSC Advances

PAPER

View Article Online
View Journal | View Issue

Cite this: *RSC Adv.*, 2026, **16**, 8735

Comparative adsorption of levofloxacin by Cu–Fe layered double hydroxides and mixed oxides: kinetics, isotherms, mechanisms, energy efficiency, and green valorization of waste adsorbents

Asmaa S. Hassan,[a] Abdullah S. Alawam,[b] Ahmed A. Allam,[b] Samar M. Mahgoub,[c] Mohamed Refat[d] and Rehab Mahmoud *[a]

The increasing prevalence of levofloxacin (LV) and related antibiotics in aquatic systems constitutes a critical environmental and public health concern, driving the need for advanced water treatment solutions. This investigation focuses on the synthesis and characterization of a copper-iron layered double hydroxide (Cu–Fe LDH) and its calcined mixed oxide derivative (Cu–Fe MO), assessing their performance as adsorbents for aqueous LV. Comparative analysis elucidates their respective removal efficiencies and underlying sequestration mechanisms. The maximum adsorption capacity for LV was quantified as 45.474 mg g^{-1} on Cu–Fe LDH at 25 °C, increasing to 59.216 mg g^{-1} at 55 °C. In contrast, the Cu–Fe mixed oxide (MO) exhibited lower capacities of 31.386 mg g^{-1} and 38.68 mg g^{-1} at 25 °C and 55 °C, respectively. These Langmuir-derived q_{max} values represent the definitive adsorption capacities for performance evaluation. Analysis of the statistical monolayer model's parameters provided insights into the adsorption energy, active site density, and saturation capacity per functional group. Theoretically, the data suggest a multi-layer adsorption mechanism with a vertical molecular orientation on the LDH surface, whereas LV adopts both vertical and horizontal alignments at the 96.4 kg^{-1} interface. Thermodynamic parameters revealed spontaneous, endothermic adsorption behavior. The observed energy range of 18.29–21.4 kJ mol^{-1} for Cu–Fe LDH and 18.05–20.9 kJ mol^{-1} for Cu–Fe MO implies that the binding mechanism evolves from physisorption at ambient temperature toward chemisorption at elevated temperatures. The practical viability of both composites was demonstrated through four regeneration cycles, highlighting their robust reusability for complex wastewater matrices. An evaluation of the procedural environmental impact, conducted *via* the AGREEprep, ESA, and AMVI green metrics, substantiated the method's alignment with sustainable principles. The electrocatalytic performance of the synthesized materials for methanol oxidation was notably enhanced following their application in adsorption. The Cu–Fe LDH composite exhibited an increase in current density from 107 mA cm^{-2} to 189.12 mA cm^{-2} post-adsorption. A similar trend was observed for the Cu–Fe MO, which showed a rise from an initial ~96 mA cm^{-2} to 146.03 mA cm^{-2} after the adsorption cycle. From an economic perspective, the manufacturing cost was estimated at $94.2 per kilogram of the Cu–Fe LDH composite.

Received 23rd November 2025
Accepted 2nd February 2026

DOI: 10.1039/d5ra09055e

rsc.li/rsc-advances

1. Introduction

Levofloxacin (LV), a widely utilized fluoroquinolone antibiotic, is valued for its broad-spectrum efficacy in human and veterinary medicine.[1] However, its pervasive application has led to significant environmental contamination, resulting in the frequent identification of LV residues across diverse ecological matrices.[2,3] The presence of LV in the environment poses significant ecological and public health risks.[4] Consequently, the development of effective remediation strategies for LV-contaminated wastewater represents a critical priority in environmental science. The establishment of efficient and cost-effective remediation methodologies is a fundamental prerequisite for the successful elimination of antibiotic contaminants from the environment.

Numerous strategies, spanning biological,[5] chemical,[6] and physical[7] processes such as biodegradation and photocatalysis, have been assessed for antibiotic remediation. However, persistent

[a]*Chemistry Department, Faculty of Science, Beni-Suef University, Beni-Suef 62511, Egypt. E-mail: rehabkhaled@science.bsu.edu.eg; dr.sma.sayed@gmail.com*

[b]*Department of Biology, College of Science, Imam Mohammad Ibn Saud Islamic University (IMSIU), Riyadh 11623, Saudi Arabia. E-mail: aallam@imamu.edu.sa; asalawam@imamu.edu.sa*

[c]*Materials Science and Nanotechnology Department, Faculty of Postgraduate Studies for Advanced Sciences, Beni-Suef University, Egypt*

[d]*Chemistry Department, Faculty of Science, Cairo University, Egypt*

drawbacks—including high cost, complexity, and the potential for secondary pollution—have limited their widespread application.[8] Consequently, adsorption technology has garnered significant attention as a promising solution to these impediments.[9]

The search for advanced adsorbents has highlighted layered double hydroxides (LDHs), which are anionic clays featuring adjustable composition and interlayer chemistry. These materials are increasingly recognized for their high surface area, structural versatility, and efficient ion exchange. Upon calcination, LDHs undergo structural collapse, transforming into mixed oxides with high crystallinity and stability, while often maintaining memory effect and surface reactivity.

Copper–iron LDH (Cu–Fe LDH) and its mixed oxide derivative (Cu–Fe MO) are particularly attractive due to the synergistic properties of Cu and Fe ions, which enhance redox activity, surface charge adaptability, and binding affinity toward organic pollutants. However, systematic studies comparing the adsorption behavior of LV on Cu–Fe LDH *versus* Cu–Fe MO remain scarce.

This investigation successfully established a synthesis protocol for a cost-effective Cu–Fe layered double hydroxide (LDH), which demonstrated high efficacy in sequestering levofloxacin (LV) from aqueous media. The synthesized adsorbent underwent rigorous physicochemical characterization *via* XRD, FTIR, BET, TG/DTG, FESEM and HRTEM. Process optimization was achieved through a Box-Behnken design integrated with response surface methodology, while equilibrium data were interpreted using Langmuir and Freundlich isotherm models. Furthermore, the adsorption mechanism was elucidated at a macroscopic scale through statistical physics modeling, which provided steric and energetic parameters. Thermodynamic analysis of entropy, Gibbs free energy, and internal energy across a temperature range confirmed the process's viability. Collectively, this multi-faceted methodology—encompassing synthesis, characterization, optimization, and theoretical modeling—validates the Cu–Fe LDH as a sustainable and efficient adsorbent for LV remediation.

2. Experimental section

2.1 Chemicals and reagents

Copper nitrate trihydrate (Cu $(NO_3)_2 \cdot 3H_2O$), ferric nitrate nonahydrate (Fe $(NO_3)_3 \cdot 9H_2O$) were obtained from Sigma-Aldrich (Missouri, United States). Sodium hydroxide (NaOH), 37% hydrochloric acid (HCL)were purchased from Scharlau (Barcelona, Spain) absolute ethanol was obtained from Merck KGaA (Darmstadt, Germany). Levofloxacin (LV, 99.86% purity) was sourced from Aarti Drugs Ltd (Mumbai, India). All solutions were prepared using deionized water.

2.2 Preparation of Cu–Fe LDH

The Cu–Fe LDH was synthesized by a co-precipitation method. An aqueous solution containing Cu^{2+} and Fe^{3+} nitrates (molar ratio 5 : 1) with 0.50 M from $Cu(NO_3)_2 \cdot 6H_2O$ and 0.10 M Fe $(NO_3)_3 \cdot 9H_2O$ was prepared under constant magnetic stirring in 200 mL with a sonication frequency of 40 kHz and a power of 305 W for 15 min was mixed with slowly added solution of 0.5 mol L^{-1} of NaOH under constant stirring, maintaining the pH at 10. The resulting suspension was aged at 70 °C for 24 h, then it was centrifuged to separate the formed precipitate which was then washed several times with deionized water then once

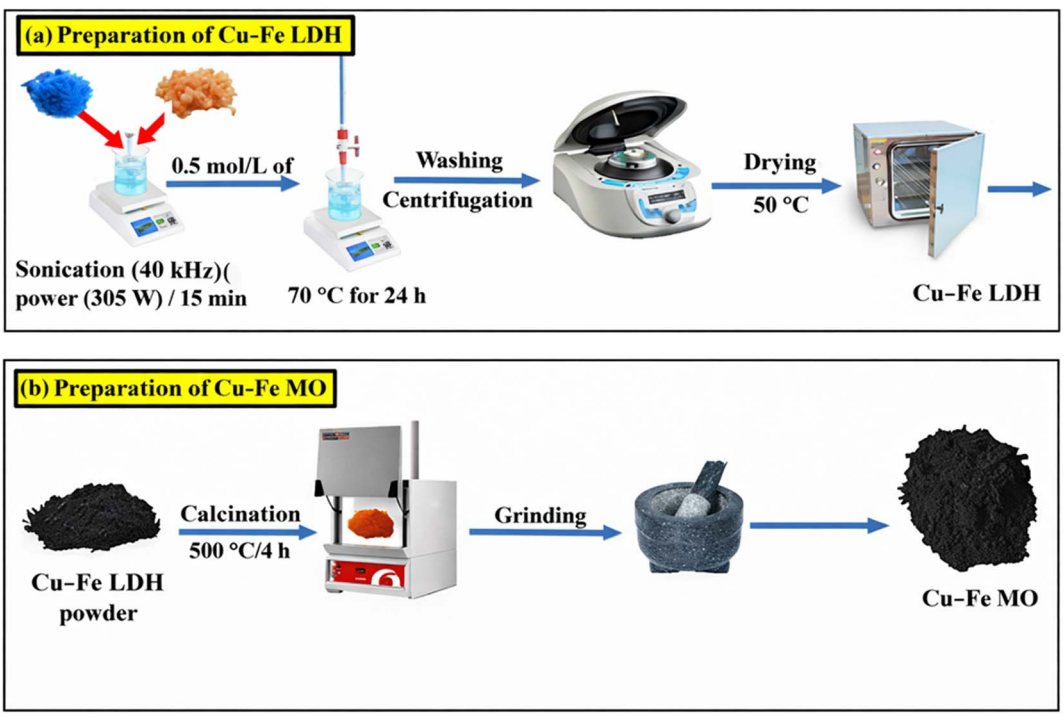

Fig. 1 (a) The procedural sequence for synthesizing the Cu–Fe LDH material and (b) the procedural sequence for synthesizing the Cu–Fe mixed oxide.

with ethanol till pH reaches 7 and then it has been left for complete dryness in the oven at 50 °C for 24 h (Fig. 1a).

2.3 Preparation of Cu–Fe mixed oxide

Approximately 2 g of the pristine LDH powder was placed in a ceramic crucible and calcined in a muffle furnace. The temperature was raised to 500 °C at a heating rate of 5 °C min^{-1} and held for 4 h under a static air atmosphere. After calcination, the furnace was allowed to cool down naturally to room temperature. The resulting solid was collected, ground, and stored in a desiccator. This product was labeled as Cu–Fe MO (Fig. 1b).

2.4 Characterization of the prepared materials

The mineralogical composition of the fabricated adsorbents was determined using X-ray diffraction (XRD) on a PANalytical Empyrean platform. This instrument, featuring a Cu Kα radiation source ($\lambda = 0.154$ nm), was configured at 40 kV and 30 mA to acquire scans across a 2θ range from 5° to 80°. Complementary analysis of functional groups was performed by Fourier Transform Infrared Spectroscopy (FTIR) using a Bruker Optics VERTEX 70 spectrometer, which recorded spectra within the 400 to 4000 cm^{-1} wavenumber window. Moreover, the surface morphology of the synthesized adsorbents was examined using a field-emission scanning electron microscope (FE-SEM, Gemini Zeiss Sigma 500 VP) operated at an accelerating voltage of 5 kV and a working distance of approximately 5 mm. The zeta potential measurements were carried out using a Zetasizer Nano instrument (Zeta-Meter Plus 3.0, Malvern Panalytical Ltd, Malvern, UK) to evaluate the surface charge and colloidal stability of the samples. Thermogravimetric analysis (TGA) was performed using a Netzsch STA 409 PC/PG at a heating rate of 10 °C min^{-1} under a nitrogen atmosphere to investigate the thermal stability of the materials. The residual drug concentration was quantitatively determined using a UV-vis spectrophotometer (Evolution 350, Thermo Fisher Scientific, Massachusetts, USA). High-resolution transmission electron microscopy (HR-TEM, JEM-2100, JEOL, Japan) was employed at an accelerating voltage of 200 kV, with a spatial resolution of 0.20 nm. High-magnification images (50×–6 00 000×) were acquired along with selected area electron diffraction (SAED) patterns to examine the crystalline structure. Lattice fringes and interplanar spacings (*d*-values) of the crystalline domains were determined using Fast Fourier Transform (FFT) analysis. Elemental analysis was performed *via* atomic absorption spectroscopy (AAS), while textural properties, including specific surface area and pore architecture, were determined from nitrogen physisorption isotherms. These microscopic and spectroscopic techniques collectively provided critical insights into the structural and compositional features of the layered double hydroxide (LDH) and mixed oxide (MO) materials.

2.5 Adsorption study

Batch adsorption studies were performed to systematically evaluate the capacity of Cu–Fe LDH and Cu–Fe MO composites for LV removal from aqueous media. The influence of pivotal operational conditions, encompassing pH (3–9), adsorbent dosage, contact time, and initial LV concentration, was thoroughly examined to optimize the decontamination process. The experimental protocol involved triplicate adsorption measurements in 50 mL centrifuge tubes under controlled settings, emphasizing pH adjustment across acidic to weakly alkaline regimes to quantify its impact on uptake behavior. For adsorption equilibrium determination, LV concentrations ranged from 10 to 1000 mg L^{-1} at constant temperatures of 25 and 55 °C. Kinetic profiles were established using 50 mL LVsolutions sampled at time points between 5 and 180 minutes. A uniform agitation velocity of 200 rpm was maintained throughout all experimental runs to guarantee homogeneous mixing. Following the adsorption phase, the residual LV concentration in the centrifuged supernatant was determined spectrophotometrically. The corresponding adsorption capacities at equilibrium (q_e) and at time t (q_t) were subsequently computed using eqn (1) and (2), respectively.

$$q_e = (C_0 - C_e)\frac{V}{m} \quad (1)$$

$$q_t = (C_0 - C_e)\frac{V}{m} \quad (2)$$

In this notation, C_0, C_e, and C_t correspond to the initial, equilibrium, and time-variant LV concentrations (mg L^{-1}). The symbols V and m denote the solution volume (L) and the mass of adsorbent (g) employed in the study.

2.6 Modelling of LV adsorption

To fully clarify the adsorption mechanisms for aquatic pollutants, the intrinsic physicochemical parameters of equilibrium models must be rigorously assessed. The Langmuir and Freundlich isotherm models serve as principal analytical frameworks in environmental research, given their proven capacity for accurately representing empirical adsorption data under varied conditions.[10,11] A rigorous, multiscale examination of sorption phenomena necessitates methodologies grounded in statistical physics.[12,13] This paradigm, which couples empirical observation with theoretical constructs, provides an unparalleled foundation for mechanistic deduction. Full experimental protocols for kinetic and equilibrium analyses are available in the SI.

2.7 Experimental design

For the multivariate enhancement of LV adsorption across two separate systems containing Cu–Fe LDH and Cu–Fe MO composites, the BBD-RSM approach represents a proficient strategy that minimizes experimental workload. The current investigation applied the Box–Behnken Design to elucidate the

Table 1 Codes and actual variables and their levels in BBD

Codes	Variables	Level 1 (−1)	Level 2 (0)	Level 3 (+1)
A	Dose (g)	0.01	0.05	0.09
B	pH	3	6	9
C	Time (min)	5	92.5	180

influence of three key operational parameters—sorbent mass, pH, and contact duration—on the removal performance of levofloxacin. This investigation employed Design Expert 12.0 (Stat-Ease) for experimental design generation. The specific value ranges assigned to the independent variables for LV adsorption are catalogued in Table 1. The collective effect of these parameters on removal efficacy was modelled through the quadratic equation provided in eqn (3).

$$Y = \beta_0 + \Sigma\ \beta_i\ X_i + \Sigma\ \beta_{ii}\ X_i^2 + \Sigma\Sigma\beta_{ij}\ X_i\ X_j \quad (3)$$

In this model, Y corresponds to the LV removal efficiency (%), while X_i and X_j denote the independent variables. The constant term is represented by β_0, with β_i, β_{ij}, and β_{ii} signifying the linear, interaction, and quadratic coefficients, respectively. The experimental design, comprising three variables and the corresponding LV removal response, is presented in Table 2. For the adsorption assays, 25 mL of LV solution was combined with a predetermined adsorbent mass in a 50 mL Falcon tube, followed by agitation at 200 rpm for a designated duration. Following the adsorption process, the adsorbent was separated from the aqueous phase by filtration through a 0.45 μm membrane. The resulting filtrate was subsequently analyzed for residual LV concentration using a HACH DR 2800 UV-vis spectrophotometer, with absorbance measurements recorded at a wavelength of 505 nm. The decolorization efficiency, corresponding to LV removal, was subsequently calculated employing eqn (4).

$$R\% = \frac{C_0 - C_e}{C_0} \times 100 \quad (4)$$

2.8 Desorption and recyclability

To assess reusability—a critical metric for practical adsorbent deployment—a regeneration study was conducted. LEV was quantitatively desorbed from the material's surface using a 0.1 M NaOH solution. This process effectively restored the adsorbent's original characteristics, confirming its potential for multiple application cycles. Regeneration potential was assessed by treating LEV-saturated adsorbent (150 mg L^{-1}) with 30 mL NaOH under ambient agitation for one hour. Following centrifugal separation and supernatant analysis, the material was washed and reused across multiple cycles. Desorption efficiency, calculated batchwise using eqn (4), verified that the material's renewability aligns with sustainable resource management paradigms by facilitating repeated application.

Table 2 The 3-variables BBD matrix and experimental data for LV removal (%)

				Cu–Fe LDH	Cu–Fe MO
Run	A: Dose (g)	B: pH	C: Time (min)	LV removal (%)	LV removal (%)
1	0.05	6	92.5	92.47	80.47
2	0.01	6	5	31.39	21.85
3	0.05	6	92.5	91.48	79.48
4	0.01	9	92.5	36.74	24.74
5	0.05	6	92.5	90.38	77.19
6	0.05	6	92.5	93.17	80.28
7	0.05	3	5	34.79	22.79
8	0.05	9	5	39.97	27.97
9	0.01	6	180	80.94	68.94
10	0.05	6	92.5	92.18	80.18
11	0.05	9	180	63.75	49.19
12	0.01	3	92.5	29.72	19.28
13	0.09	6	180	98.27	87.15
14	0.09	6	5	68.23	56.18
15	0.09	3	92.5	54.37	40.92
16	0.09	9	92.5	57.194	44.18
17	0.05	3	180	61.48	47.92

2.9 Valorization of spent adsorbent

2.9.1 Fabrication of the working electrode. To prepare the working electrode, 5.0 mg of the spent adsorbent material—previously utilized in adsorption experiments—was uniformly dispersed in a solvent mixture containing 380 μL of isopropanol and 20 μL of a 4.0 wt% Nafion solution. The resulting suspension underwent ultrasonic agitation for 20 minutes to ensure homogeneous dispersion of particles and to minimize agglomeration, which is essential for achieving reliable and reproducible electrochemical performance. After sonication, a 20 μL aliquot of the suspension was precisely drop-cast onto a pre-cut graphite paper substrate (1 cm × 1 cm; thickness: 1.5 mm). The modified electrode was then air-dried at room temperature to facilitate solvent evaporation and promote the formation of a stable catalytic layer.

2.9.2 Electrochemical measurements. Electrochemical testing of the modified electrodes was carried out using a Metrohm AUTOLAB PGSTAT 302 N potentiostat/galvanostat, operated through NOVA 1.11 software. All measurements were conducted in a conventional three-electrode configuration within a glass electrochemical cell at ambient temperature. The reference electrode used was Ag/AgCl (saturated KCl), the counter electrode was a platinum wire, and the working electrode consisted of the prepared and spent adsorbent-coated graphite paper. The electrocatalytic performance of the modified electrodes was evaluated in an alkaline medium of 1 M KOH, both in the absence and presence of urea at varying concentrations, to mimic practical electrocatalytic scenarios. Cyclic voltammetry (CV) was performed over a potential window of 0 to 1 V *versus* Ag/AgCl, with scan rates ranging from 5 to 60 $mV \cdot s^{-1}$, to study the redox behavior and extract kinetic information related to the electrocatalytic process. In addition, chronoamperometric (CA) measurements were conducted at a constant potential of 1.0 V for a duration of 1 hour, aiming to assess the long-term stability. The time-dependent current response obtained from CA analysis provides valuable insight into the practical applicability of the catalyst, especially for sustained urea oxidation reactions.

3. Results and discussion

3.1 Structural and morphological characterization

The successful synthesis of Cu–Fe LDH and its thermal transformation to Cu–Fe mixed oxide (MO) was confirmed through

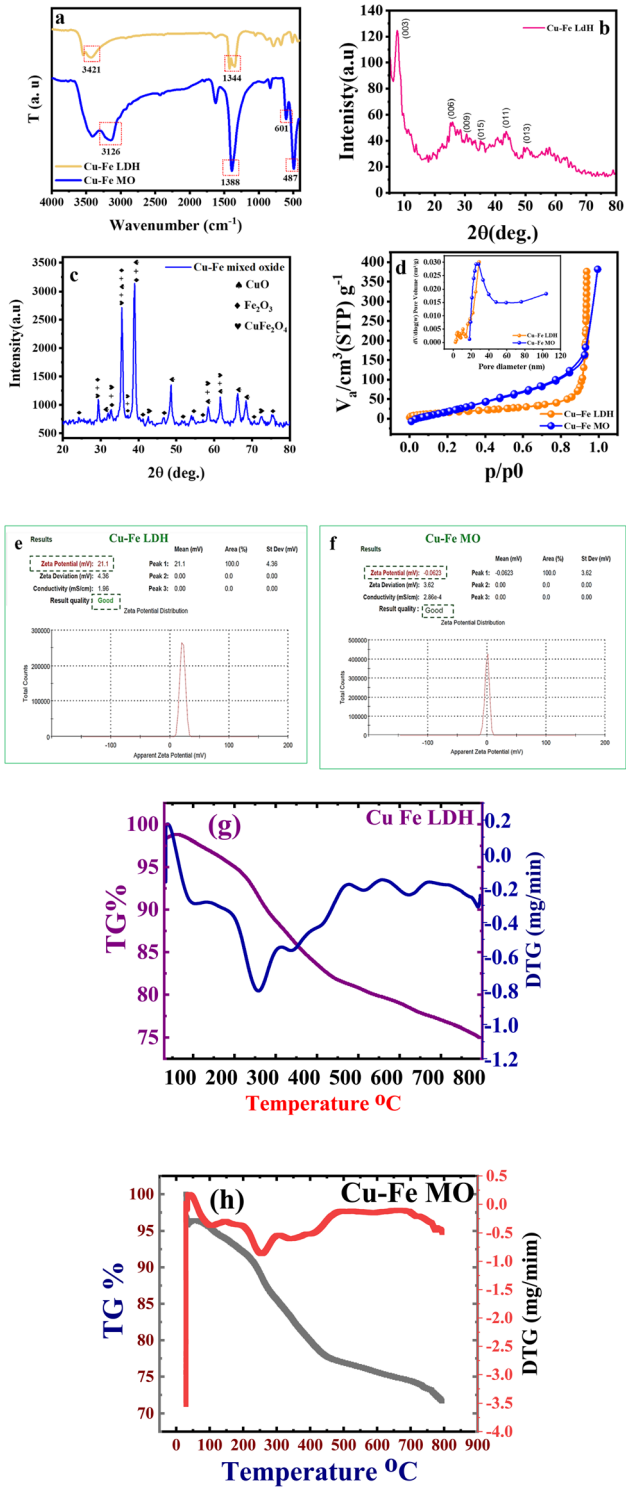

Fig. 2 (a) FTIR spectra of Cu–Fe LDH and Cu–Fe MO, (b and c) XRD of LDH and MO prepared materials respectively, (d) BET surface area of Cu–Fe LDH and Cu–Fe MO, (e and f) Zeta potential of the prepared samples and (g and h) thermal analysis (%TG and DTG) of prepared materials.

comprehensive characterization techniques. Fourier-transform infrared (FTIR) spectroscopy (Fig. 2a) revealed characteristic vibrational patterns for both materials. The Cu–Fe LDH spectrum exhibited a broad absorption band at approximately 3421 cm^{-1}, corresponding to O–H stretching vibrations of interlayer water molecules and hydroxyl groups in the brucite-like layers. A sharper band at 1380 cm^{-1} confirmed the presence of nitrate anions in the interlayer galleries, balancing the positive charge of the metal hydroxide sheets.[14] Additional metal–oxygen (M–O) vibrations appeared below 800 cm^{-1}, consistent with typical hydrotalcite-like structures.[15]

Upon calcination at 500 °C, the FTIR spectrum of Cu–Fe MO showed significant changes: the disappearance of the interlayer water and nitrate vibrations indicated structural decomposition, while new metal–oxygen–metal (M–O–M) vibrations emerged below 700 cm^{-1}, characteristic of mixed metal oxides.[16] This transformation confirms the complete conversion of the layered structure to a crystalline oxide phase through thermal treatment.

X-ray diffraction (XRD) analysis (Fig. 2b) provided further evidence of the structural evolution. The Cu–Fe LDH pattern displayed characteristic reflections at 2θ = 7.8°, 25.6°, 30.4°, 35.1°, 43.8°, and 50.5°, corresponding to (003), (006), (009), (015), (011), and (013) planes, respectively, of a well-crystallized hydrotalcite-like phase.[17] The basal spacing calculated from the (003) reflection was approximately 11.6 Å, consistent with reported LDH structures containing nitrate anions.[18] The crystallite size, estimated using the Scherrer equation, was approximately 9.20 nm.

After calcination, the XRD pattern of Cu–Fe MO showed complete disappearance of LDH reflections and the emergence of new peaks attributable to crystalline oxide phases (Fig. 2c). Peaks at 2θ = 29.3°, 35.6°, 37.2°, 46.8°, 54.1°, 58.4°, and 61.7° were indexed to the (220), (331), (222), (400), (422), (511), and (440) planes of a spinel-type $CuFe_2O_4$ phase (JCPDS #77-0010).[19] Additional reflections at 24.3°, 35.6°, 39.0°, 42.5°, 48.5°, 54.1°, and 58.4° corresponded to the (012), (104), (110), (113), (024), (116), and (018) planes of Fe_2O_3 (hematite, JCPDS #33-0664), while peaks at 32.0°, 35.6°, 37.2°, 39.0°, 48.5°, 58.4°, 61.7°, 66.2°, 68.5°, and 75.5° matched the (110), (111), (022), (202), (202), (113), (022), (220), (222), and (201) planes of CuO (tenorite, JCPDS #45-0937).[20] The increased crystallite size (10.5 nm) and enhanced peak sharpness indicated improved crystallinity after calcination, resulting from removal of volatile components and atomic rearrangement into more stable oxide phases.[21]

Nitrogen adsorption–desorption isotherms provided quantitative information on the textural properties (Fig. 2d). Cu–Fe LDH exhibited a type IV isotherm with an H3-type hysteresis loop, indicating mesoporous characteristics with a specific surface area of 82 $m^2\ g^{-1}$.

The calcined Cu–Fe MO showed a similar isotherm type but with increased surface area (105 $m^2\ g^{-1}$) and wider pore size distribution, suggesting enhanced surface heterogeneity resulting from the decomposition of layered structure and formation of mixed oxides.[15] This increase in surface area following calcination has been observed in other LDH-derived systems and contributes to the adsorption capabilities of the material (Table 3).[22]

Zeta potential analysis was investigated and represented in Fig. 2 (e and f). Cu–Fe LDH, which exhibits a positive zeta potential of +21.1 mV with a narrow distribution (standard

deviation ≈ 4.36 mV). This positive surface charge related to the charged brucite-like layers of LDHs, resulting from partial substitution of Cu^{2+} and Fe^{3+} cations and charge compensation by interlayer anions.[23] The relatively high positive zeta potential indicates good colloidal stability due to electrostatic repulsion and confirms the successful formation of the LDH structure. On the other hand, the zeta potential of the Cu–Fe mixed oxide (MO) shows a value close to neutrality (−0.06 mV) with a slightly narrower deviation (≈3.62 mV). The near-zero negative zeta potential suggests the loss of layered structure and surface hydroxyl charge upon calcination, leading to reduced electrostatic stabilization and a higher tendency toward particle aggregation.[24] This behavior is characteristic of mixed metal oxides, whose surface charge is strongly dependent on pH and typically approaches neutrality near their isoelectric point. The marked shift from a strongly positive zeta potential in Cu–Fe LDH to an almost neutral value in Cu–Fe MO provides clear experimental evidence of the structural transformation from LDH to mixed oxide. Moreover, the positively charged surface of Cu–Fe LDH is advantageous for the adsorption of negatively charged species and facilitates interfacial reactions, while the neutral surface of Cu–Fe MO may favor redox-driven catalytic processes rather than electrostatic interactions.

As shown in Fig. (2g), the thermogravimetric profile illustrates the characteristic thermal behavior of layered double hydroxides (LDHs). The initial weight loss observed below approximately 150 °C is attributed to the removal of physically adsorbed moisture and interlayer water molecules.[25] The second, more pronounced mass loss occurring in the temperature range of 150–300 °C corresponds to the release of strongly bound interlayer water, accompanied by the onset of dehydroxylation of the LDH layers, as confirmed by the associated minimum in the DTG curve.[26] The continuous weight loss detected between ∼300 and 500 °C is assigned to further dehydroxylation of the metal hydroxide layers and the decomposition of interlayer anions, resulting in progressive destabilization of the layered structure. A broader decomposition region extending from ∼500 to 700 °C reflects the complete collapse of the LDH framework and the formation of mixed metal oxide phases. Beyond ∼700 °C, the TG curve exhibits a markedly reduced mass loss rate, indicating the development of thermally stable oxide species.[27]

The thermogravimetric analysis (TGA) profile of the Cu–Fe mixed oxide (MO) is presented in Fig. 2h. Several distinct weight-loss regions can be observed, reflecting the thermal behavior, stability, and compositional transformations of the material.[28] The initial slight weight loss occurring below 100 °C is attributed to the removal of physically adsorbed moisture and residual surface-bound water molecules. The second weight-loss stage, evidenced by a DTG peak at approximately 251 °C, corresponds to the elimination of chemisorbed water and the decomposition of residual hydroxyl groups or nitrate species originating from the precursor salts used during synthesis.[27] A more pronounced mass loss observed around 345.5 °C is associated with the decomposition of intermediate metal hydroxides or oxyhydroxides and the subsequent formation of the stable Cu–Fe mixed oxide phase through solid–state interactions between copper and iron species. Beyond 411 °C, the TGA curve becomes nearly horizontal, indicating high thermal stability of the Cu–Fe mixed oxide. The absence of further significant weight loss confirms the successful formation of a thermally stable oxide structure.[29]

Scanning electron microscopy (SEM) images revealed distinct morphological differences between the two materials (Fig. 3). Cu–Fe LDH exhibited a characteristic layered architecture with plate-like nanoparticles aggregated into flower-like microspheres, creating a highly accessible surface morphology with numerous interparticle voids and pores.[30] This hierarchical organization is typical of LDHs synthesized by co-precipitation methods.[30]

After calcination, Cu–Fe MO maintained a little porous framework structure but with more densely packed, interconnected flakes and reduced interlayer spacing, resulting from structural dehydration and consolidation.[31] The preservation of the overall morphology despite the phase transformation suggests a topotactic conversion process, where the precursor morphology influences the final oxide structure.

HRTEM analysis was performed to confirm the structure of the prepared materials where we can find that in Fig. 3c LDH and MO in Fig. 3d. The LDH sample exhibits platelet and layers like nanostructures with particle sizes ranging from approximately 57–124 nm, indicating a LDH morphology. However, the MO shows relatively larger, irregularly shaped and more compact nanoparticles with sizes in the range of 88–174 nm, suggesting structural collapse following thermal treatment.

3.2 Statistical modeling and interaction effects on LV removal

The model's predictive adequacy was statistically validated through analysis of variance (ANOVA) to evaluate its congruence with empirical data. As summarized in Table 4, the regression analysis yielded highly significant F-values of 62.58 ($p < 0.0001$) for the Cu–Fe LDH system and 49.28 ($p < 0.0001$) for the Cu–Fe MO system, thereby confirming the model's substantial statistical relevance.[9] A strong correlation between experimental and predicted values is evidenced by a R^2 of 0.98. Statistical significance was assigned to model terms with p-values below 0.05, indicating a substantial influence on LV removal.

Table 3 Textural properties of Cu–Fe LDH and Cu–Fe MO

Material	BET surface area ($m^2\ g^{-1}$)	SD	Pore volume ($cm^3\ g^{-1}$)	SD	Average pore size (nm)	SD
Cu–Fe LDH	82.00	±4.1	0.21	±0.02	8.50	±0.6
Cu–Fe MO	105.00	±5.3	0.28	±0.02	9.70	±0.7

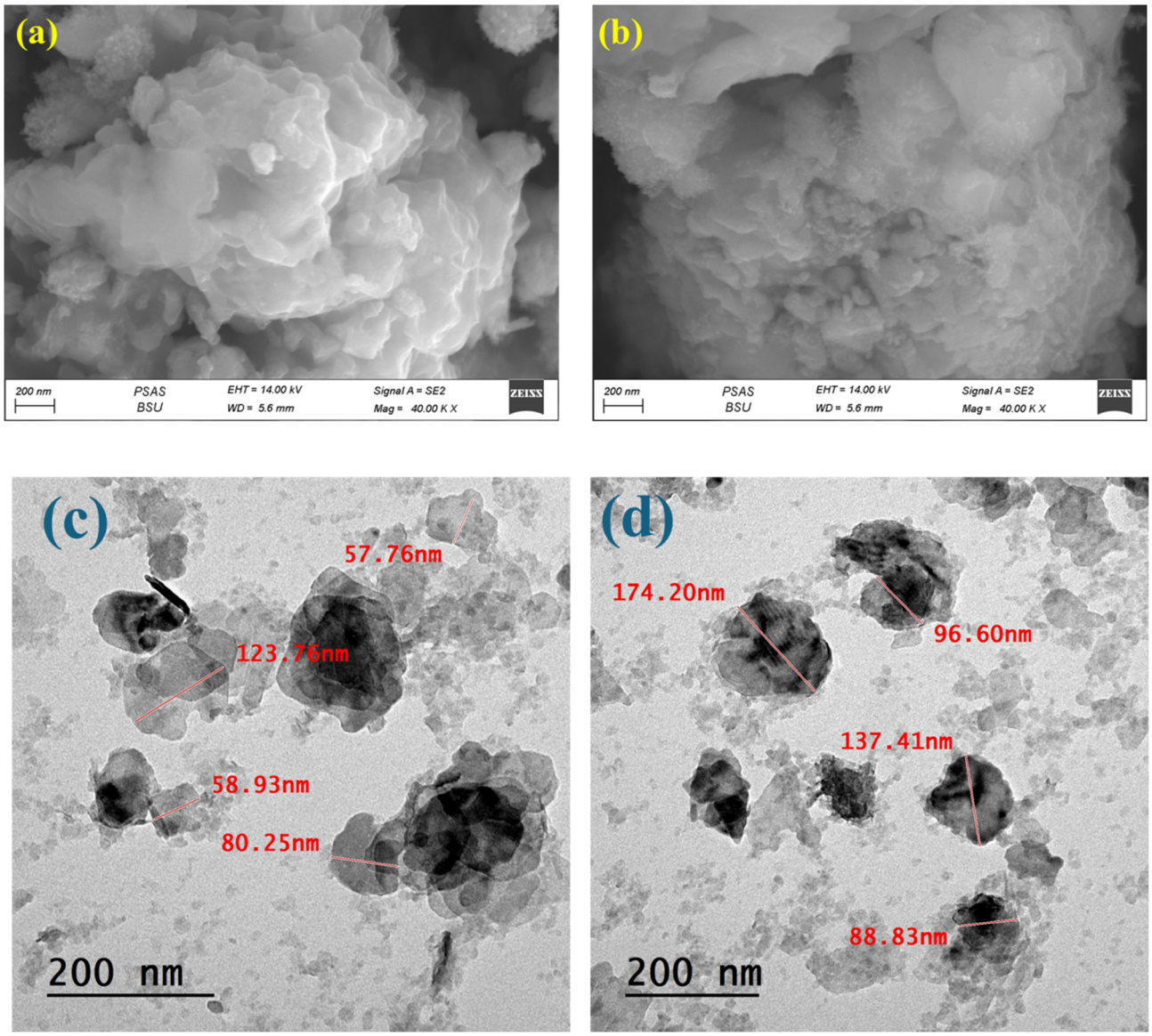

Fig. 3 FESEM micrographs of (a) LDH, (b) MO and HRTEM images for (c) LDH and (d) MO respectively.

Table 4 Analysis of variance (ANOVA) for LV removal

	Cu–Fe LDH					Cu–Fe MO				
Source	SS	d*f*	MS	*F*-value	*p*-value	SS	d*f*	MS	*F*-value	*p*-value
Model	9774.32	9	1086.04	62.58	<0.0001	9509.9	9	1056.66	49.28	<0.0001
A-dose	1231.92	1	1231.92	70.98	<0.0001	1095.59	1	1095.59	51.09	0.0002
B-pH	37.39	1	37.39	2.15	0.1856	28.77	1	28.77	1.34	0.2847
C-time	2114.45	1	2114.45	121.84	<0.0001	1934.73	1	1934.73	90.23	<0.0001
AB	4.4	1	4.4	0.2536	0.63	1.21	1	1.21	0.0564	0.819
AC	95.16	1	95.16	5.48	0.0517	64.96	1	64.96	3.03	0.1253
BC	2.12	1	2.12	0.122	0.7372	3.82	1	3.82	0.1782	0.6856
A^2	808.84	1	808.84	46.61	0.0002	694.04	1	694.04	32.37	0.0007
B^2	4745.03	1	4745.03	273.41	<0.0001	4982.93	1	4982.93	232.39	<0.0001
C^2	294.87	1	294.87	16.99	0.0044	279.76	1	279.76	13.05	0.0086
Residual	121.48	7	17.35			150.1	7	21.44		
Lack of fit	116.99	3	39	34.69	0.0025	142.75	3	47.58	25.91	0.0044
Pure error	4.5	4	1.12			7.35	4	1.84		
Cor total	9895.8	16				9659.99	16			

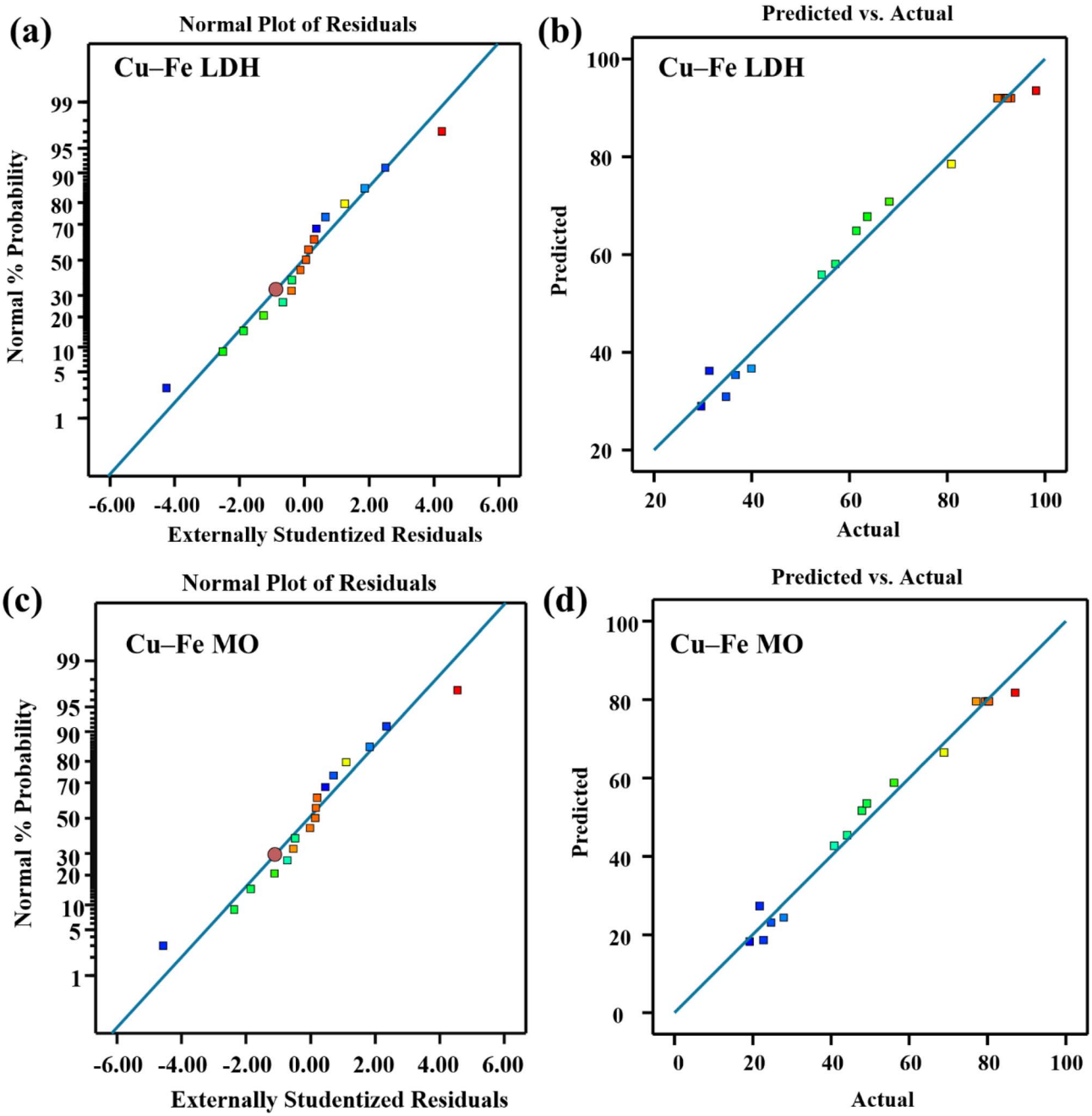

Fig. 4 (a and c) Normal probability plot of residuals for LV removal and (b and d) the plot of the relationship between the predicted and actual values of LV removal.

Consequently, the linear terms A and C, alongside the quadratic terms A^2, B^2, and C^2, were identified as statistically significant for both the Cu–Fe LDH and Cu–Fe MO composites. The final regression models (eqn (4) for Cu–Fe LDH and eqn (5) for Cu–Fe MO) were formulated by excluding non-significant terms from the initial equations.[32]

$$\text{LV removal (\%)}_{\text{LDH}} = +91.94 + 12.41A + 16.26\text{C} - 13.86A^2 - 33.57B^2 - 8.37C^2 \quad (5)$$

$$\text{LV removal (\%)}_{\text{MO}} = +79.52 + 11.7A + 15.55C - 12.84A^2 - 34.4B^2 - 8.15C^2 \quad (6)$$

Residual analysis serves as a fundamental diagnostic tool for assessing model adequacy. As illustrated in Fig. 4a and c, the validation of the developed model is supported by the random distribution of residuals adjacent to the reference line, indicating that the error structure conforms to expected statistical behavior.[25] The correlation between modeled predictions and experimental outcomes for LV removal is visualized in Fig. 4b and d. The close proximity of data points to the ideal fit line confirms a robust agreement, indicating that the theoretical framework provides a reliable representation of the empirical process.[33]

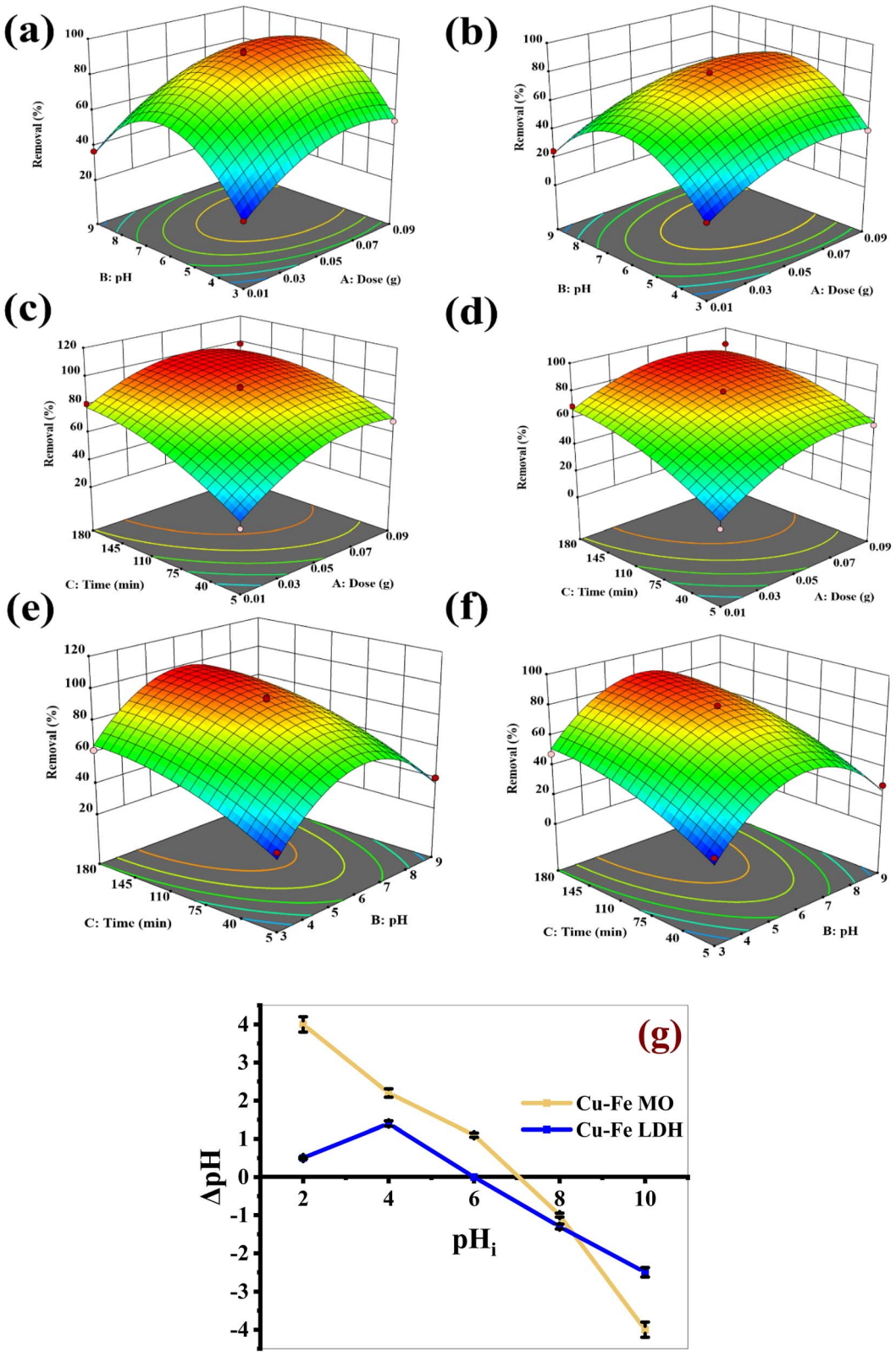

Fig. 5 3D response surfaces and 3D contour plots of (a, c and e) for LDH and (b, d and f)) for MO; while (g) pHpzc of both Cu–Fe LDH and Cu–Fe MO.

3.2.1 Effect of dual interactions. The synergistic effects of operational variables were visualized through three-dimensional surface analysis. The response surfaces illustrating the combined influence of pH and adsorbent dosage (Fig. 5a and b) demonstrate a negative relationship, with LV removal efficiency increasing progressively across the pH

range of 3 to 9. It's known that, LV exhibits three acid dissociation constants (pKa_1 = 5.91, pKa_2 = 8.21, pKa_3 = 11.74),[34] which govern its speciation as a cationic species below pH 5.91, a zwitterion between pH 5.91 and 8.21, and an anionic form above pH 8.21.[4] Complementarily, the point of zero charge (pH_{pzc}) was measured at 6.80 for Cu–Fe LDH and 6.10 for Cu–Fe MO (Fig. 5g), with the lower value for the mixed oxide confirming a more acidic surface character following thermal treatment. Based on the determined pH_{pzc} values, the surfaces of Cu–Fe LDH and Cu–Fe MO are protonated and carry a positive charge at pH levels below 6.80 and 6.10, respectively. Under these acidic conditions, favorable electrostatic interactions with anionic LV species are promoted. Consequently, a pH of 6.0 was identified as the optimum for LV sequestration, balancing surface charge with adsorbate speciation.

As evidenced in Fig. 5c and 7d, the sequestration efficiency demonstrated a positive correlation with adsorbent mass, exhibiting enhancement as the dosage of both Cu–Fe LDH and Cu–Fe MO was increased from 0.01 to 0.09 g. This performance improvement is attributable to the proportional expansion of available surface area and the corresponding increase in reactive sites provided by greater adsorbent quantities. Three-dimensional response surface analysis (Fig. 5c and d) elucidates the synergistic relationship between adsorbent dosage and contact duration on LV sequestration. The results demonstrate a positive temporal correlation, with removal efficiency escalating substantially as interaction time increases from 5 to 180 minutes. This kinetic profile reflects the diffusion-controlled migration of LV molecules through the internal pore architecture of both Cu–Fe LDH and Cu–Fe MO composites.

3.2.2 Adsorption kinetics. To characterize the adsorption behavior of LV molecules, experimental kinetic data were fitted to Pseudo-First-Order (PFO),[35] Pseudo-Second-Order (PSO),[36] Elovich,[37] and Intraparticle Diffusion (IPD)[38] models. Interpreting the data through this comprehensive framework clarifies the underlying rate-controlling processes and informs subsequent optimization of the material's design and application. The adsorption kinetics were interpreted through PFO and PSO models to evaluate performance and mechanism. The PFO

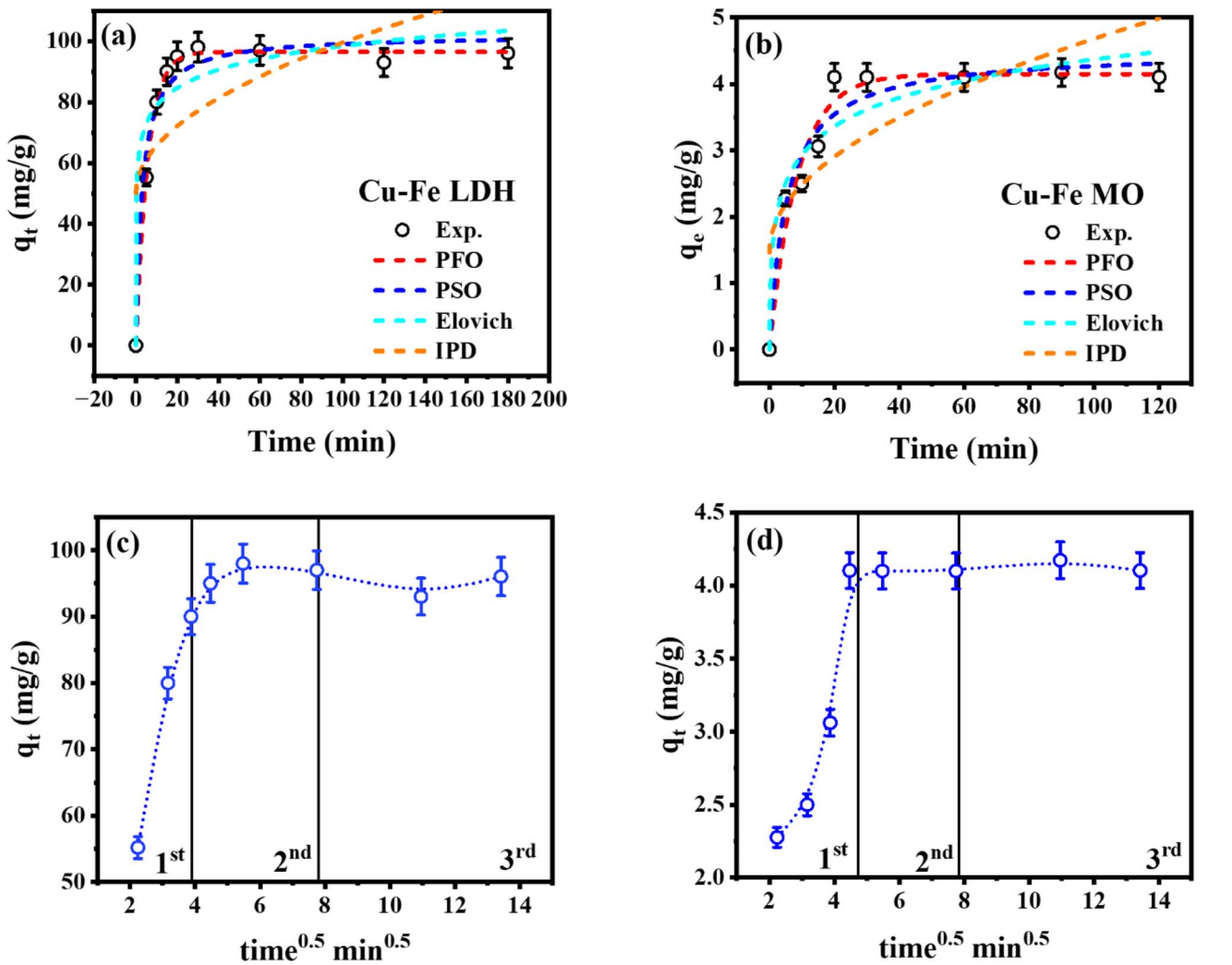

Fig. 6 (a) Adsorption kinetic models, (b) scheme of kinetic adsorption, (c) IPD model, and (d) schematic diagram of diffusion LV into prepared materials.

model provides a valid assessment of the adsorption timeline, relevant for application scaling. Conversely, the PSO model's alignment with the data indicates that chemical interaction is the rate-limiting step, simultaneously yielding the maximum adsorption capacity value presented in Table S3. For processes on heterogeneous surfaces, the Elovich model reveals critical information on site energy distribution and kinetic trends amidst changing solute concentrations. Deploying a combination of kinetic models yields a multi-faceted perspective on LV uptake, from which optimal operational settings for pollutant removal can be established. The synergistic application of these kinetic frameworks substantially augments the reliability of adsorption evaluations, facilitates the exact calibration of operational parameters, and directs the formulation of effective treatment protocols for metallic effluents. This multifaceted analytical approach concurrently clarifies essential sequestration mechanisms and advances the engineering of superior sorbent substances, as conceptually summarized in Fig. 6a for Cu–Fe LDH and 6b for Cu–Fe MO.

The PFO kinetic model offers a critical framework for elucidating the adsorption behaviour of LV onto the Cu–Fe sorbents and for evaluating their operational performance. The model, which features rate constants (K_1) of 0.175 min^{-1} for Cu–Fe LDH and 0.12 min^{-1} for Cu–Fe MO, is exceptionally useful for interpreting the early adsorption stages. These quantified kinetic data on LV removal are crucial for informing the enhancement of decontamination strategies for pharmaceutical-laden effluents. The magnitude of the K_1 constant implies a deliberate initial adsorption phase for the Cu–Fe sorbents, which transitions into a high cumulative LV loading capacity. Leveraging this kinetic insight allows for the precise adjustment of operational parameters like exposure time and contaminant concentration to elevate removal efficacy. Consequently, this empirical characterization of the adsorption timeline provides a scientific basis for subsequent iterations in material design and process optimization.[35]

Application of the PSO kinetic framework provides essential insight into the adsorption dynamics and functional efficacy of

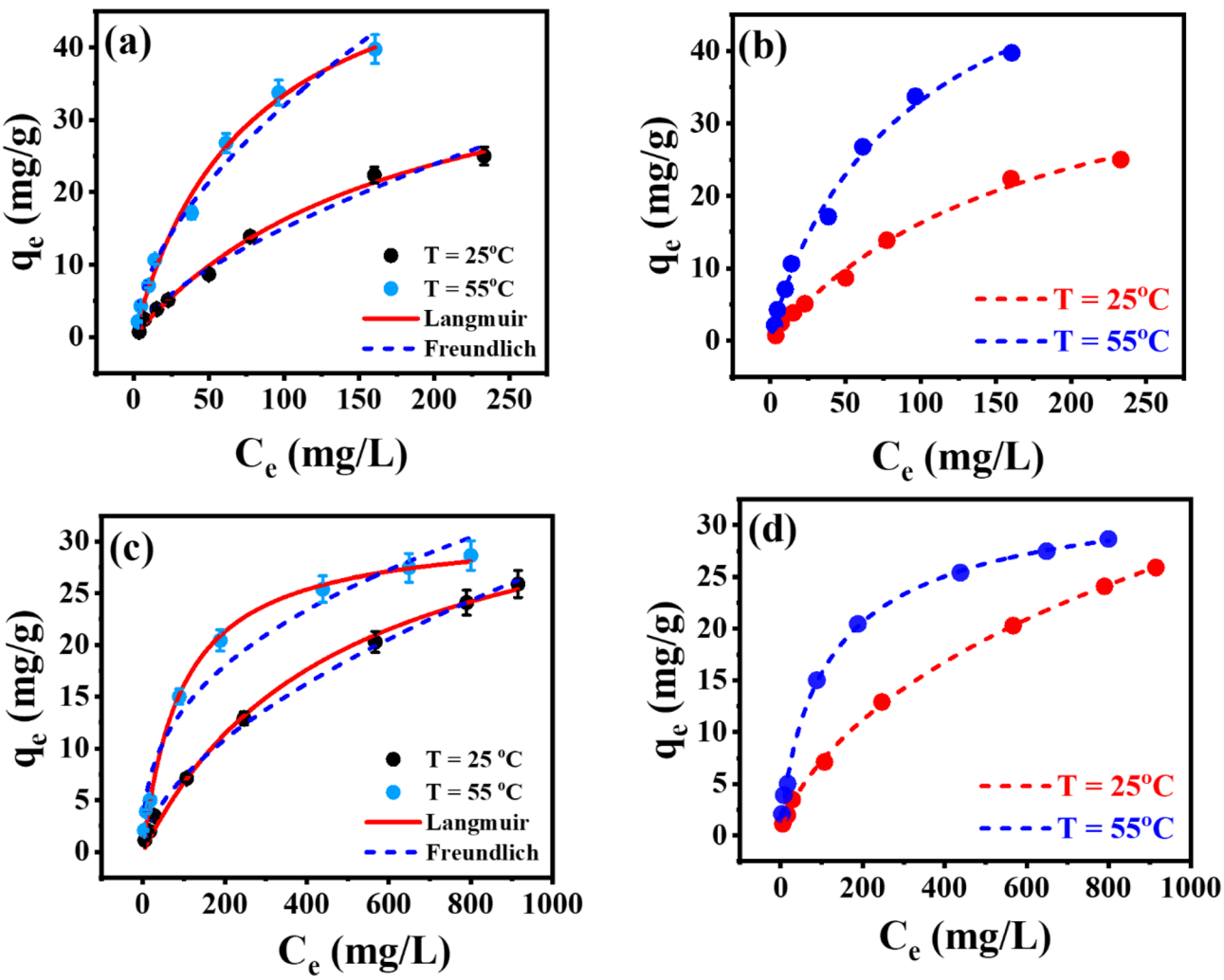

Fig. 7 Equilibrium adsorption isotherms for levofloxacin (LV) uptake onto Cu–Fe LDH and Cu–Fe MO composites at different temperatures. (a and b) Represent LV adsorption onto Cu–Fe LDH at 25 and 55 °C, while (c and d) correspond to Cu–Fe MO under identical conditions. Experimental data are fitted using the Langmuir (solid lines) and Freundlich (dashed lines) models, illustrating the temperature-dependent adsorption behavior and the enhanced adsorption capacity at elevated temperature. All experiments were conducted at solution pH = 7.0.

the sorbents. The model's fit, characterized by rate constants (K_2) of 0.0032 $g \cdot mg^{-1} \cdot min^{-1}$ for Cu–Fe LDH and 0.041 $g \cdot mg^{-1} \cdot min^{-1}$ for Cu–Fe MO, indicates a process whose velocity is governed by chemisorption phenomena, as corroborated in Table S3. This correlation confirms that the adsorption rate exhibits a second-order dependence on the concentration of available reactive sites, thereby validating a chemisorption-dominated mechanism.[36]

The findings underscore the robust affinity between Cu–Fe LDH and Cu–Fe MO's functional groups and LV ions, providing critical insight into the fundamental adsorption processes. The diminished K_2 value signifies the LV adsorption rate, serving as a key parameter for assessing the long-term performance of Cu–Fe LDH and Cu–Fe MO. This kinetic model reveals the optimal adsorption capacity, a critical factor in determining both the required contact duration and initial LV concentration for maximum removal efficiency. Such kinetic analysis proves indispensable for real-world implementation across varying LV concentrations, offering valuable data for improving the sorptive performance of hydrogel-based adsorbents (Fig. 6a).

The Intraparticle Diffusion (IPD) kinetic model facilitates a detailed investigation of the LV sequestration process on the Cu–Fe composites. This analytical approach yields essential information on the underlying adsorption mechanisms and the materials' remedial efficacy. With calculated diffusion rate constants (K_p) of 4.95 $mg \cdot g^{-1} \cdot min^{0.5}$ for Cu–Fe LDH and 0.322 $mg \cdot g^{-1} \cdot min^{0.5}$ for Cu–Fe MO, the model clarifies the solute transport dynamics within the porous frameworks, underscoring the critical role of intraparticle diffusion in the overarching adsorption pathway. The demonstrated removal efficiency is paramount for maximizing contaminant extraction and enabling swift pollutant immobilization in aqueous treatment systems. Equilibrium isotherm analysis identified maximal LV uptake capacities of 50.03 mg g^{-1} for Cu–Fe LDH and 1.462 mg g^{-1} for Cu–Fe MO, highlighting their significant sequestration potential. Furthermore, kinetic profiling using the Intraparticle Diffusion (IPD) model discriminates between rate-determining steps—specifically, film diffusion *versus* transport within the nanofibrous pore structure—yielding essential diagnostic information on process constraints.[38] The IPD Kinetic Model serves a dual purpose: it augments the mechanistic interpretation of sorption dynamics while concurrently calibrating key process conditions to maximize contaminant recovery. Such an integrated framework substantially propels the innovation of sustainable remediation techniques for wastewater containing pharmaceutical compounds.

Employing the Elovich model advances the mechanistic understanding of adsorption on heterogeneous solids. Derived constants for Cu–Fe LDH ($\alpha = 0.12$, $\beta = 8903.813$) and Cu–Fe MO ($\alpha = 1.595$, $\beta = 6.654$) delineate the energy distribution of active sites, highlighting their distinct surface interaction characteristics. Within the Elovich framework, the β parameter denotes the theoretical maximum uptake of LV by the Cu–Fe composites, underscoring their pronounced efficacy in pharmaceutical sequestration from aqueous streams.[37] Concurrently, the α coefficient characterizes the initial adsorption velocity; its moderate magnitude indicates protracted contaminant removal, aligning with the system's inherent kinetic constraints. This understanding is operationally critical for treating waste streams with inconsistent antibiotic concentrations, providing a pragmatic basis for process assessment. The Elovich analysis refines the mechanistic portrayal of the specific interactions at the Cu–Fe interface, an approach that concurrently clarifies sequestration phenomena and advances the development of efficient remediation solutions, highlighting its importance in applied environmental science.

3.2.3 Diffusion mechanism. The sequestration of LV by the Cu–Fe composites follows a tripartite transport mechanism. The initial stage involves film diffusion, where a concentration gradient drives molecular migration across the hydrodynamic boundary layer enveloping the adsorbent particles (Fig. 6c and d). Subsequently, pore diffusion governs the gradual percolation of LV through the macroporous architecture, with kinetic rates diminishing as internal diffusion distances increase. The terminal stage represents saturation, marked by near-complete site occupancy and the eventual establishment of a dynamic adsorption–desorption equilibrium.

3.3 Isotherm studies

The equilibrium isotherm studies were conducted at pH 7.0, while the BBD optimization identified pH 6.0 as the operational optimum. This choice is justified by several practical and scientific considerations: (1) environmental relevance, as pH 7.0 represents neutral conditions commonly encountered in

Table 5 Simple equilibrium model parameters resulted from LV uptake by Cu–Fe LDH and Cu–Fe MO

		Parameters					
Material	Isotherm model	T (°C)	q_{max} (mg g^{-1})	K_L (L mg^{-1})	R^2	X^2	RMSE
Cu–Fe LDH	Langmuir	25	45.474	0.006	0.994	0.500	0.657
		55	59.216	0.013	0.986	0.875	1.184
	Freundlich		K_F	$1/n_F$			
		25	0.696	0.667	0.985	1.676	1.035
		55	2.202	0.581	0.981	2.861	1.821
Cu–Fe MO	Langmuir	25	31.386	0.0021	0.998	0.250	0.390
		55	38.68	0.0106	0.996	0.912	0.661
	Freundlich		K_F	$1/n_F$			
		25	0.502	0.581	0.995	1.283	0.673
		55	2.4231	0.378	0.969	4.050	1.825

natural and treated waters; (2) adsorbate stability, ensuring LV ($pKa_1 = 5.91$, $pKa_2 = 8.21$) remains predominantly in its stable zwitterionic form throughout the extended equilibrium experiments, minimizing pH-related degradation or speciation changes; and (3) literature comparability, as neutral pH serves as a standard benchmark for adsorption studies.

The response surface analysis (Fig. 5a and b) demonstrates that removal efficiency remains high across the pH range of 6–7, with both pH values falling within the optimal region of the response surface. Visual inspection of the contour projections indicates minimal variation in removal percentage between pH 6.0 and 7.0 when other parameters are held constant. The slight pH shift therefore has negligible impact on adsorption capacity, ensuring that the reported isotherm parameters reliably reflect the materials' performance under near-neutral conditions representative of practical applications.

This study probed the adsorption mechanism governing LV uptake by Cu–Fe LDH and Cu–Fe MO through a comprehensive isotherm analysis. The equilibrium data were interpreted using both conventional isotherms (Langmuir, Freundlich) and sophisticated statistical physics models (monolayer, double-layer) to provide multi-scale insight into the solid–liquid interface.

3.3.1 Simple equilibrium models. The Langmuir and Freundlich models were applied to characterize LV uptake by the Cu–Fe composites at two temperatures (Fig. 7 and Table 5). Due to the comparable and high R^2 values (>0.98) exhibited by both models, the Chi-square (χ^2) and RMSE metrics were employed to discriminate the model with the superior fit to the experimental data. Statistical evaluation using the χ^2 and RMSE tests confirmed the Langmuir isotherm's superior fit for both composites at all experimental temperatures. These results suggest LV removal proceeds through uniform active sites on the adsorbent surfaces, leading to the formation of a single molecular layer. Langmuir-derived q_{max} values for Cu–Fe LDH increased from 45.474 mg g^{-1} at 25 °C to 59.2161 mg g^{-1} at 55 °C, while Cu–Fe MO exhibited a more substantial enhancement from 31.386 to 38.68 mg g^{-1} over the same temperature range

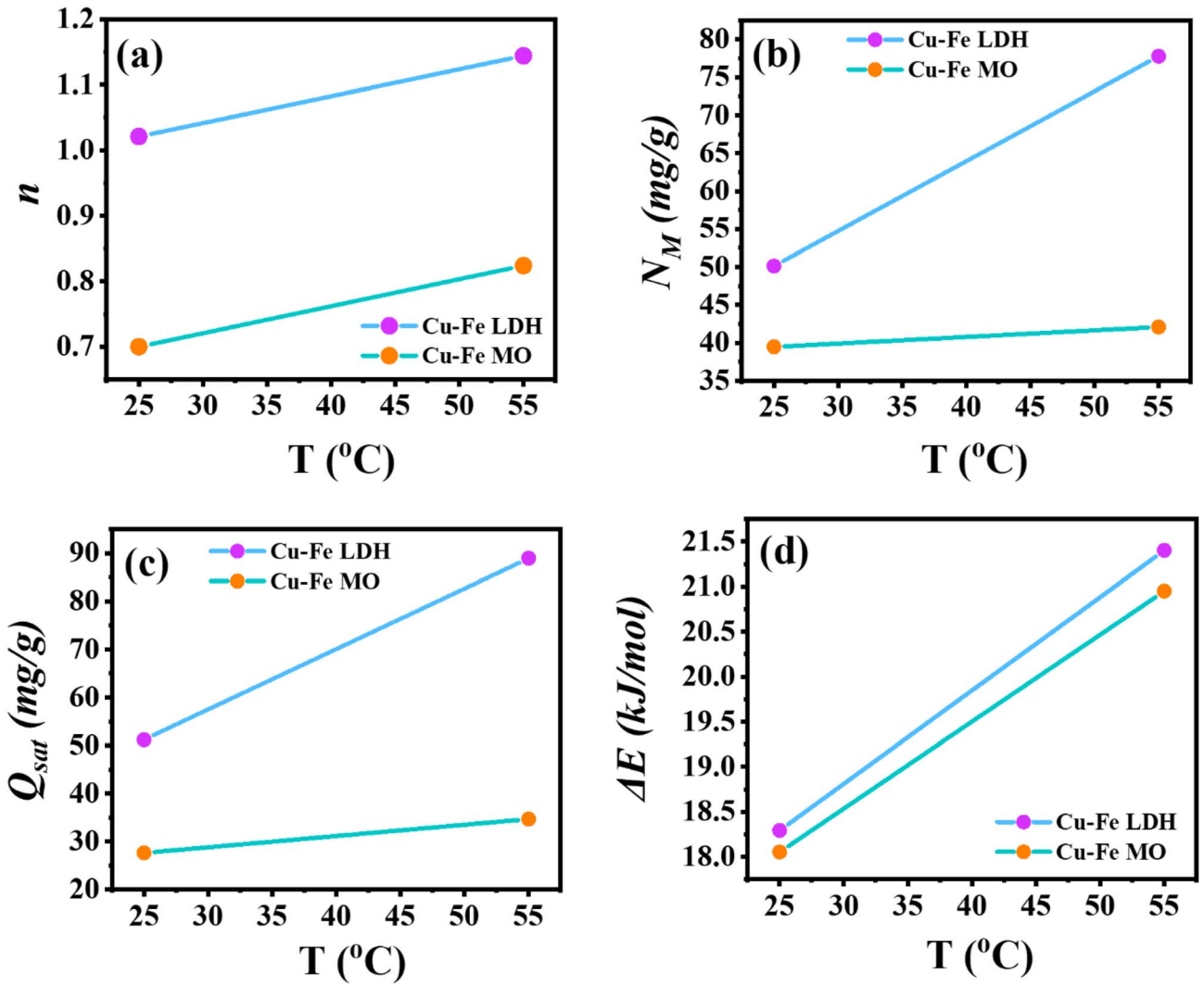

Fig. 8 Steric (n, N_M, Q_{sat}) and energetic (ΔE) parameters of AMM *vs.* temperature for LV adsorption on Cu–Fe LDH or Cu–Fe MO composites at different solution temperatures.

(Table 5). This positive correlation between adsorption capacity and temperature signifies an endothermic mechanism, thereby confirming that higher temperatures facilitate superior adsorption performance for the LV-composite system. A systematic increase in the Freundlich affinity coefficient (K_F) from 0.696 to 2.202 (mg g^{-1}) (mg L^{-1})$^{-1/n}$ for Cu–Fe LDH while Cu–Fe MO exhibited a more substantial enhancement from 0.502 to 2.4231 (mg g^{-1}) (mg L^{-1})$^{-1/n}$ with elevated temperature provided additional evidence of endothermic adsorption behavior. The consistently observed $1/n_F$ values of less than 1.0 further indicated a highly favorable adsorption isotherm, demonstrating strong LV-composite interactions even in dilute solutions.[39,40] For comparative assessment with other adsorbents, the Langmuir q_{max} values (Table 5) should be considered the definitive maximum adsorption capacities.

3.3.2 Complex equilibrium models. The mechanistic understanding of adsorption processes remains constrained when relying solely on classical isotherm models, whose parameters often possess ambiguous physical meaning.[39] A more profound elucidation of the interfacial behavior between LV and the Cu–Fe composites can be achieved by applying sophisticated physical formalisms that quantify steric arrangements, energy landscapes, and thermodynamic driving forces.[41,42] The application of statistical physics principles to determine steric and energetic parameters yields profound mechanistic insights. Collectively, these advanced models provide a robust theoretical foundation for analyzing adsorption phenomena, thereby substantially advancing the fundamental comprehension of aqueous remediation systems.[42]

3.4 Interpterion of the adsorption mechanism *via* the best complex adsorption model

The experimental data for LV adsorption demonstrated optimal conformity with the advanced monolayer model (AMM), exhibiting R^2 values exceeding 0.99 and RMSE values of 1.17–1.69 for Cu–Fe LDH and 2.48–3.15 for Cu–Fe MO. As illustrated in Fig. 6b and d, the AMM provides an accurate representation of the adsorption equilibrium across the entire temperature range investigated. Critical steric and energetic parameters including the number of adsorbate molecules per site (n), receptor site density (N_M), saturation capacity (Q_{sat}), and adsorption energy (ΔE)—were subsequently evaluated to elucidate the fundamental sequestration mechanism.[42–44]

3.4.1 Steric (n, NM, and Q_{sat}) parameters. The parameter, *n*, provides critical insight into the interfacial dynamics and spatial configuration of LV during its adsorption onto Cu–Fe LDH and Cu–Fe MO. The magnitude of this exponent delineates three distinct adsorption modalities, each defined by a specific interaction mechanism and molecular orientation. An *n* value below 0.5 characterizes the first regime, where adsorption proceeds *via* a multi-docking mechanism. In this scenario, LV molecules engage with numerous active sites on the adsorbent surface, resulting in a predominantly horizontal orientation. The second regime, identified by an *n* parameter between 0.5 and 1, corresponds to a heterogeneous adsorption process. Within this range, LV molecules adopt a mixed geometry, exhibiting both vertical and horizontal alignments on the adsorbent's surface. The final regime, signified by an *n* value greater than 1, points to a cooperative, multi-molecular adsorption mechanism. This condition favors a vertical

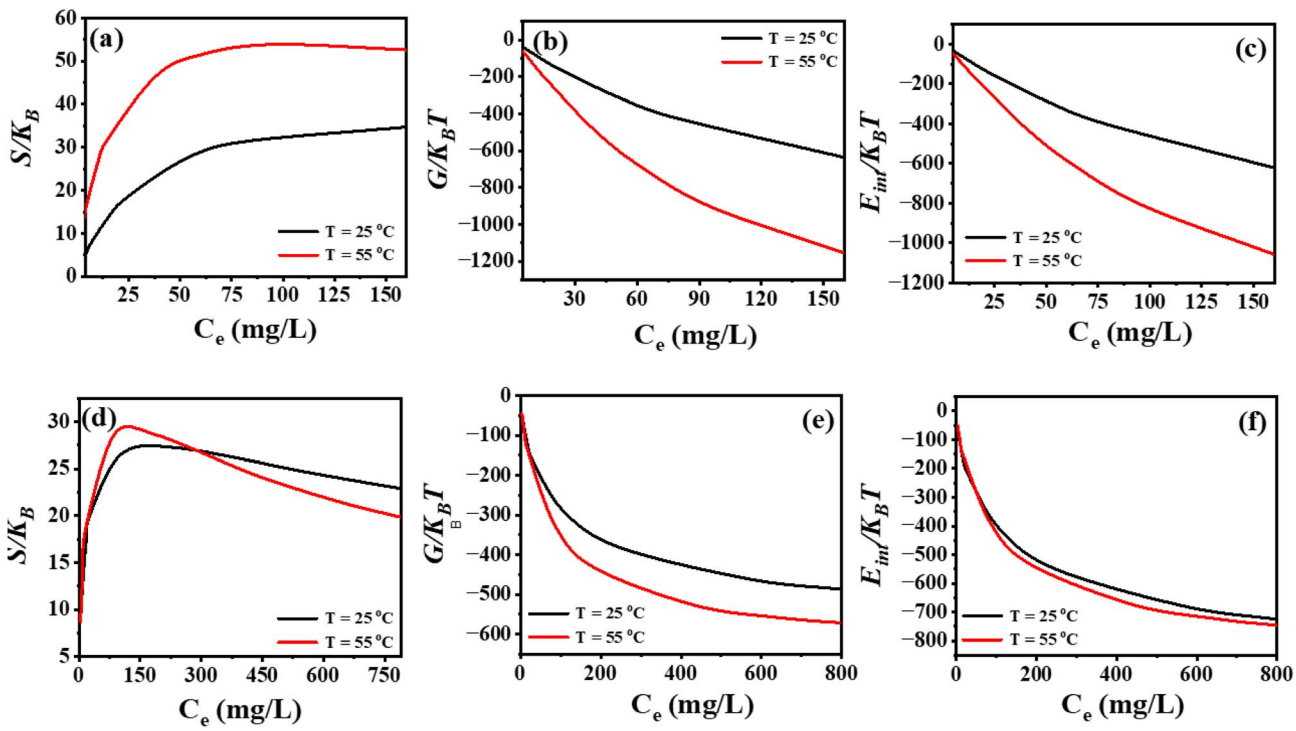

Fig. 9 Thermodynamic study of LV ions uptake by (a–c) Cu–Fe LDH and (d–f) Cu–Fe MO at 25 and 55 °C for (a–d) entropy, (b–e) Gibbs free energy, and (c–f) internal energy.

orientation of the LV molecules, suggesting the formation of adsorbate layers at the solid–liquid interface. Fig. 8 illustrates the influence of rising solution temperature on the parameter *n*, with corresponding numerical data detailed in Table S2. For the Cu–Fe LDH adsorbent, the *n* parameter was determined to be 1.012 at 25 °C and 1.144 at 55 °C. In contrast, the values for Cu–Fe MO were 0.7001 and 0.828 at the respective temperatures. The consistent observation of *n* > 1 for Cu–Fe LDH across the studied thermal range indicates a uniform adsorption mechanism and a stable molecular orientation. This finding corroborates a multi-molecular adsorption process with a vertical geometry for the LV–Cu–Fe LDH interaction throughout the temperature interval from 25 to 55 °C. In the context of Cu–Fe MO, the *n* resides within the range of 0.5 to 1, signifying a heterogeneous adsorptive process. This specific regime is characterized by a mixed molecular orientation, wherein LV molecules arrange in both vertical and horizontal alignments at the solid–liquid interface. Notably, the adsorption is preceded by a solution-phase aggregation phenomenon involving LV–LV intermolecular association. Moreover, elevated temperatures were found to exert no significant influence on the configuration of the adsorbed LV species or the nature of their interactions with the active sites of either the Cu–Fe LDH or Cu–Fe MO adsorbents.

The density of active sites (NM) for both Cu–Fe LDH and Cu–Fe MO was evaluated across a temperature gradient, with the resultant data presented in Fig. 8. As quantified in Table S2, the NM parameter demonstrates a pronounced thermal dependence. Specifically, the value for Cu–Fe LDH increases substantially from 50.143 mg g^{-1} at 25 °C to 77.764 mg g^{-1} at 55 °C. A more modest augmentation from 39.48 mg g^{-1} to 42.104 mg g^{-1} is observed for Cu–Fe MO over the same temperature range. The observed positive correlation between temperature and active site density (N_m) suggests that thermal energy facilitates the generation of new adsorption sites within the composite matrices of Cu–Fe LDH and Cu–Fe MO. This phenomenon enhances the materials' capacity for LV uptake. A concurrent increase in the *n* with temperature further substantiates this mechanism, indicating a shift toward a more multi-molecular (vertical) adsorption geometry. This shift implies that the adsorbent's functional capacity is not merely a function of its inherent surface area but is also dynamically enhanced by the thermally-promoted aggregation of LV molecules in solution, which subsequently access and occupy newly available sites on the composite surface.

Within the applied multi-molecular adsorption model, the theoretical saturation capacity (Q_{sat}) is quantitatively defined by the relationship $Q_{sat} = n \times N_M$.[45,46] The accurate determination of this parameter is fundamental for a rigorous assessment of adsorbent performance. Experimental data obtained across a temperature range of 25 to 55 °C reveal a pronounced thermal enhancement of the saturation uptake for LV. Specifically, the Q_{sat} value for Cu–Fe LDH increased from 51.196 to 88.962 mg g^{-1}, while the value for Cu–Fe MO rose from 27.641 to 34.694 mg g^{-1}, a trend corroborated by the datasets in Fig. 8 and Table S3. The notable augmentation in adsorption capacities observed at higher temperatures points to the formation of robust interactions between LV molecules and the functional groups present on the Cu–Fe LDH and Cu–Fe MO adsorbents. This thermally enhanced uptake provides further confirmation of the endothermic nature of the adsorption process, indicating that the binding of LV to the active sites requires a net input of thermal energy to proceed efficiently. The observed positive correlation between temperature and LV uptake can be attributed to enhanced molecular mobility at elevated temperatures. This increased kinetic energy facilitates more effective diffusion and interaction of LV molecules with the primary receptor sites, both on the surface and within the porous matrix of the Cu–Fe LDH and Cu–Fe MO adsorbents. This thermal effect is further substantiated by the concurrent rise in both the saturation capacity (Q_{sat}) and the n parameter, as detailed in Table S3. The parallel increase in these parameters indicates that the adsorptive performance is predominantly governed by the steric considerations encapsulated by the n parameter, which dictates the available site density and molecular orientation. It is important to note that the Q_{sat} values derived from the AMM ($n \times N - M^{-}$) are theoretical saturation capacities based on a multi-molecular adsorption mechanism and are therefore higher than the experimentally-fitted Langmuir q_{max} values. The Langmuir q_{max} remains the appropriate metric for comparing maximum uptake performance across different studies.

3.4.2 Energetic parameters. Interpretation of the LV adsorption mechanism on Cu–Fe LDH and Cu–Fe MO was achieved by computing the adsorption energy parameter (ΔE). The Advanced Monolayer Model (AMM) framework provided the energetic values associated with single-layer formation at discrete temperature intervals.

$$C_{SH} = C_S\, e^{-\frac{\Delta E}{RT}} \quad (7)$$

where C_S is the LV solubility, and C_{SH} is the concentration at half-saturation.

The thermodynamic parameter ΔE, representing the adsorption energy, was quantified across a temperature gradient of 25 °C to 55 °C, with the results detailed in Fig. 8 and Table S3. The consistently positive magnitude of ΔE across this thermal spectrum confirms the endothermic nature of the LV sequestration process on both Cu–Fe LDH and Cu–Fe MO composites.[41] At ambient temperature (25 °C), the calculated ΔE values remained below the 20 kJ mol^{-1} threshold, indicative of a physisorption mechanism governed by electrostatic attractions and hydrogen bonding. A progressive increase in temperature to 55 °C, however, corresponded with a transition in the adsorption energy, with ΔE exceeding 20 kJ mol^{-1}. This shift signifies a change in the dominant binding mechanism toward chemisorption, characterized by stronger chemical interactions at the adsorbent–adsorbate interface.[45] A positive correlation was observed between increasing temperature (25–55 °C) and the enhancement of both the adsorption energy (ΔE) and saturation capacity (Q_{sat}). This parallel progression of energetic and steric parameters demonstrates their synergistic relationship in the adsorption process. The data confirm that the thermodynamic driving force (ΔE) played a pivotal role in

augmenting the LV sequestration capabilities of the Cu–Fe LDH and Cu–Fe MO composites.

3.4.3 Reconciliation of Langmuir monolayer assumption with multilayer behavior from statistical physics modeling. The strong fit of the Langmuir isotherm (R^2 > 0.98) to the experimental data indicates that the adsorption process can be empirically described by a model assuming homogeneous sites and monolayer saturation. However, the advanced monolayer model (AMM) from statistical physics provides a more nuanced molecular-scale interpretation. The parameter n derived from the AMM reveals that adsorption occurs *via* a multi-molecular mechanism (n > 1 for Cu–Fe LDH), suggesting that multiple LV molecules can associate with a single functional group or adsorption site, leading to a vertical orientation and potential stacking at the interface. This does not contradict the Langmuir model but rather clarifies that the "monolayer" in the Langmuir sense corresponds to saturation of available sites, each of which may accommodate more than one adsorbate molecule in a coordinated manner. Thus, while the Langmuir model offers a practical macroscopic description of adsorption capacity, the statistical physics model uncovers the underlying multilayer-type behavior at the molecular level, reconciling the empirical fit with the mechanistic reality of the adsorption process.

3.5 Thermodynamic studies

3.5.1 Entropy. The dependence of entropy on both LV concentration and thermal conditions is depicted in Fig. 9a and d. Analysis of these profiles indicates a monotonic increase in system randomness as the adsorbate load rises, reaching an apex before declining. The observed initial ascent in entropy is attributable to heightened molecular degrees of freedom near half-saturation, where translational motion of ions is maximized, preceding a transition to an ordered state at complete coverage.[45] The initial stage of adsorption was characterized by a high density of vacant active sites, facilitating substantial LV uptake. The entropy reached its maximum near the point of half-saturation, indicative of the system's peak configurational freedom. As the remaining sites became occupied, entropy decreased, with a final value of zero corresponding to a complete monolayer and the consequent cessation of molecular mobility at the interface.

3.5.2 Gibbs free energy. Thermodynamic analysis reveals a monotonic reduction in Gibbs free energy (ΔG) with increasing LV concentration, as illustrated in Fig. 9b and e. The process's spontaneity across the investigated temperature spectrum is verified by the universal negativity of ΔG.[45] Therefore, the capacity of the Cu–Fe LDH and Cu–Fe MO composite for LV sequestration is energetically self-sustaining, a critical attribute underscoring its utility for cost-efficient water purification.

3.5.3 Internal energy. The profile of internal energy (E_{int}) as a function of LV concentration, measured at 25 and 55 °C, is displayed in Fig. 9c and f. The exothermic nature of the adsorption reaction is evidenced by the negative E_{int} values, signifying a net energy transfer from the (LV + Cu–Fe LDH/Cu–Fe MO) system to the solution. The steep initial reduction in E_{int} is a direct consequence of the abundant availability of surface binding sites at the onset of the process. The more substantial decrease observed at elevated temperatures denotes an evolution to a system of superior thermodynamic stability,[45]

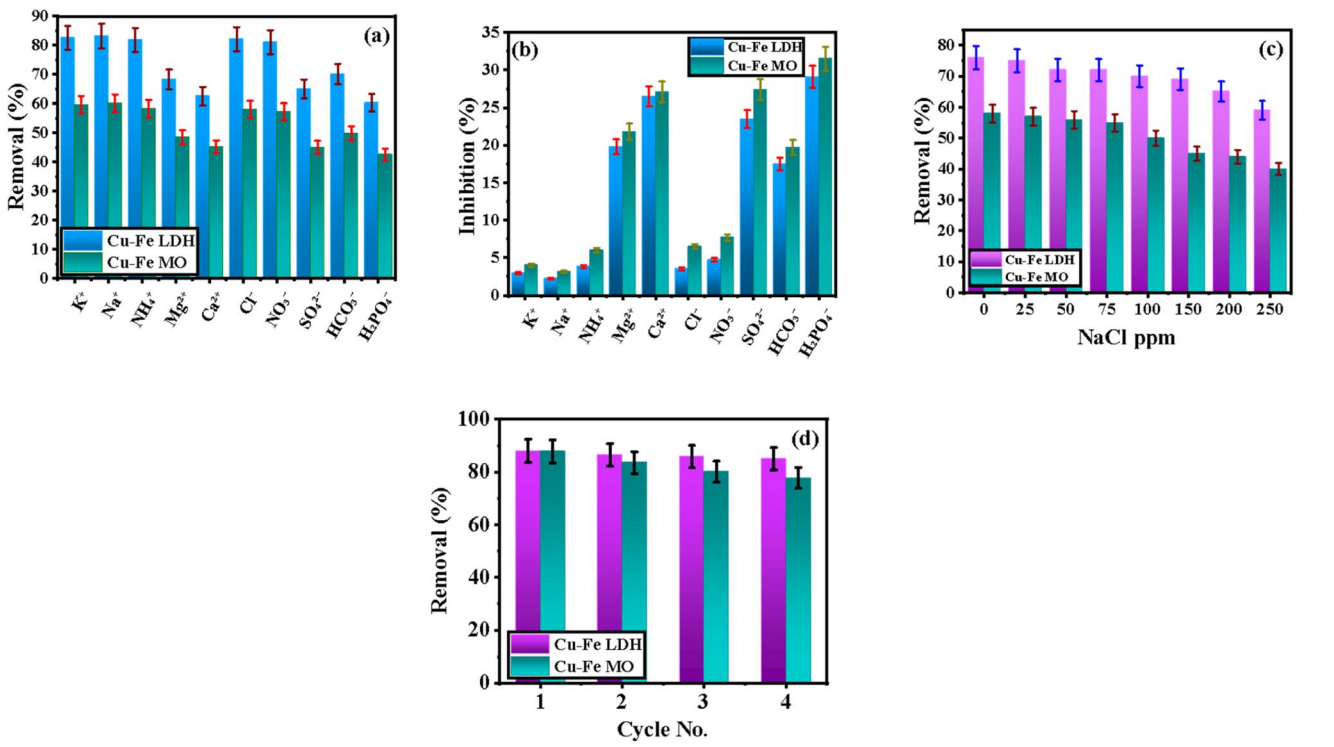

Fig. 10 (a) Effect of co-existing ions on LV adsorption efficiency, (b) inhibition (%), (c) effect of salinity, and (d) recyclability.

a phenomenon driven by enhanced thermal energy that fosters ion migration and subsequent binding.

3.6 Effect of co-existing ions

The presence of co-existing ions significantly inhibited LV adsorption, with inhibition intensity following the order $H_2PO_4^-$ > Ca^{2+} ≈ SO_4^{2-} > Mg^{2+} > HCO_3^- > other monovalent ions, reflecting a clear dependence on ion valency and specific interaction mechanisms. Divalent ions (Ca^{2+}, Mg^{2+}, SO_4^{2-}) caused substantial inhibition (19.8–27.4% for LDH; 21.8–27.4% for MO) through strong competition for adsorption sites and charge shielding effects, while $H_2PO_4^-$ demonstrated the most severe impact (29.1% for LDH; 31.5% for MO) due to its specific ability to form inner–sphere complexes with metal oxide sites. Notably, monovalent ions (Cl^-, NO_3^-, Na^+, K^+) showed minimal interference (<5% inhibition for LDH; <8% for MO), primarily through non-specific ionic strength effects. Throughout all conditions, Cu–Fe LDH consistently demonstrated superior contaminant removal and greater resilience to ionic interference compared to Cu–Fe MO, maintaining 8–23% higher absolute removal efficiency, underscoring its enhanced robustness for application in complex water matrices, as shown in (Fig. 10a and b).

3.6.1 Salinization effect. The influence of ionic strength on LV adsorption was evaluated for both Cu–Fe LDH and Cu–Fe MO adsorbents by introducing sodium chloride across a concentration gradient of 0 to 250 mg L^{-1}. Experiments utilized mixed solute solutions with a fixed LEV concentration of 150 mg L^{-1}. Results demonstrated a significant inverse relationship between ionic strength and adsorption efficacy, where increasing NaCl concentration substantially suppressed contaminant removal (Fig. 10c). A pronounced inhibitory effect on LVV removal was observed due to co-existing ions. The underlying mechanism involved direct competition, where Cl^- anions preferentially adsorbed to active sites on the Cu–Fe LDH and Cu–Fe MO matrices, effectively reducing available surface area. Concurrently, elevated salinity compressed the electrical double layer, increasing the electrostatic potential and creating a repulsive force that further disadvantaged LV adsorption. This consensus with previous studies confirms the significant role of ionic environment in modulating adsorbent performance.[47]

3.7 Regeneration and reusability

The regeneration study over four consecutive cycles demonstrated the excellent reusability and superior structural stability of Cu–Fe LDH compared to its mixed oxide derivative, as illustrated in Fig. 10d. Using 0.1 M NaOH as the eluent, Cu–Fe LDH maintained a high and stable desorption efficiency, decreasing only marginally from 88.0% in the first cycle to 85.0% in the fourth cycle, whereas Cu–Fe MO exhibited a more pronounced decline from 79.0% to 70.0% under the same conditions. This superior performance of the LDH is attributed to its robust layered structure, which better withstands the alkaline regeneration process and resists structural degradation, thereby retaining a greater proportion of its active sites. The gradual decline in efficiency for both materials is likely due to minor, irreversible binding of LVmolecules and slight structural alterations over repeated cycles; nonetheless, the high retention of capacity confirms the practical feasibility and economic viability of Cu–Fe LDH for repeated use in wastewater treatment applications.

3.8 Comparison with literature

A comparative assessment of LNV adsorption performance, detailed in Table 6, positions the Cu–Fe LDH and Cu–Fe MO composites against contemporary adsorbents based on parameters such as operational pH window, equilibrium time, cycle stability, and removal capacity. While the maximum adsorption capacities (q_{max}) of the synthesized composites are competitive, they are not the highest values reported. The significant advantage of the Cu–Fe LDH and Cu–Fe MO system lies in its balanced combination of a competitive adsorption capacity with excellent reusability (4 cycles), a synthesis protocol validated by green metrics (AGREEprep, BAGI), and a unique post-adsorption valorization pathway as an electrocatalyst. This multifunctionality and circular design are not commonly reported for the alternative sorbents listed. Reusability testing, a critical metric for assessing practical longevity, confirmed the

Table 6 Competitive for LV Adsorption using different adsorbents and the materials under study

Adsorbent	Time (min)	pH	Cycle	Q_e LV (mg g^{-1})	Ref.
UiO-66/CA	120	7	5	86.43	48
Zn–Al LDH	120	9	—	11.87	49
Nano cerium oxide wood chip biochar	120	6.5	—	73	50
Green synthesized Fe_3O_4 nanoparticles	1440	7	4	22.47	51
Fe_2O_3 (mesoporous iron oxide)	10	7.5	—	33.1	52
V_2O_5@Ch/Cu-TMA	—	3	—	11.40	53
CuO NPs	120	7	—	0.12–0.13	54
MWCNTs/$CoFe_2O_4$	90	5	6	122.2	55
FXM hydrogel	2	6.5	5	182.19	56
S-OFX	10	7	10	—	57
CMNFs–MMT	90	5	6	65.901	58
KOH-activated carbon	90	9	—	100.38	59
Cu–Fe LDH	180	7	4	59.216	This work
Cu–Fe MO	180	7	4	38.68	This work

superior cyclic stability of these materials compared to many existing alternatives. This durability, combined with their pronounced biocompatibility and cost-effectiveness, establishes the Cu–Fe composites as promising and sustainable candidates for the eco-conscious remediation of LV pollutants.

3.9 Proposed adsorption mechanism

Based on comprehensive characterization and adsorption studies, the removal of LV by Cu–Fe LDH and Cu–Fe MO is proposed to occur through a multi-mechanistic process. Electrostatic interactions between positively charged adsorbent surfaces and anionic or zwitterionic forms of LV play a significant role, particularly for Cu–Fe LDH due to its enhanced surface charge density and anion exchange capacity. Hydrogen bonding occurs between surface hydroxyl groups on the adsorbents and carbonyl, carboxylic, or hydroxyl groups of LV molecules, with stronger interactions observed for Cu–Fe LDH owing to its preserved hydroxyl groups compared to the dehydrated mixed oxide surface. Additionally, π–π interactions between the aromatic rings of LV and electron-accepting sites on the adsorbent surfaces are enhanced in Cu–Fe LDH due to its layered structure facilitating better molecular alignment. Surface complexation through coordination between LV functional groups and surface metal atoms is further supported by pH-dependent adsorption behavior and spectral evidence. Specifically, for Cu–Fe LDH, anion exchange between interlayer anions and anionic species of LV provides an additional unique mechanism. The combination of these interconnected mechanisms, enabled by the layered structure, accessible interlayer galleries, higher surface area, and greater availability of active sites in Cu–Fe LDH, collectively explains its superior adsorption performance compared to Cu–Fe MO for LV removal from aqueous solutions (Fig. 11).

3.10 Electrochemical oxidation performance of Cu–Fe LDH and MO electrodes before and after LV adsorption

3.10.1 Effect of scan rate on electrochemical oxidation. The cyclic voltammetry (CV) profiles obtained for four prepared electrodes, recorded at scan rates ranging from 5 to 60 $mV \cdot s^{-1}$, provide valuable insights into their electrochemical characteristics prior to LV adsorption. With increasing scan rate, both electrodes exhibit a proportional rise in current density. Comparative analysis reveals that the spent adsorbent electrodes consistently achieve higher current densities than LDH or MO electrode at all scan rates as shown in Fig. 12, with maximum values of approximately 1238.40 $mA \cdot cm^{-2}$ for LDH/LV and 161.96 $mA \cdot cm^{-2}$ for MMO/LV Fig. 12a–d. This enhanced performance of the LDH electrode is likely attributable to its layered, hydrated structure, which promotes ion accessibility and provides a larger electrochemically active surface area. In contrast, the more crystalline and potentially less hydrated structure of the MMO results in slightly diminished capacitive behavior. This distinction aligns with literature reports, which highlight the superior ion-exchange capacity and surface wettability of layered double hydroxides, contributing to their improved charge storage properties.

After the adsorption of LV onto the Cu–Fe LDH and Cu–Fe MMO electrodes, a marked enhancement in current response is observed across all scan rates, indicating effective interaction between the drug molecules and the electrode surfaces. For the Cu–Fe LDH/LV system, the current density increases substantially, reaching approximately 238.40 mA cm^{-2} at the highest scan rate. This nearly twofold increase compared to the pre-adsorption value suggests that LV not only adsorbs efficiently onto the LDH surface but also enhances its electrochemical activity. This improvement can be attributed to the layered and hydrated structure of LDHs, which provides a high surface area

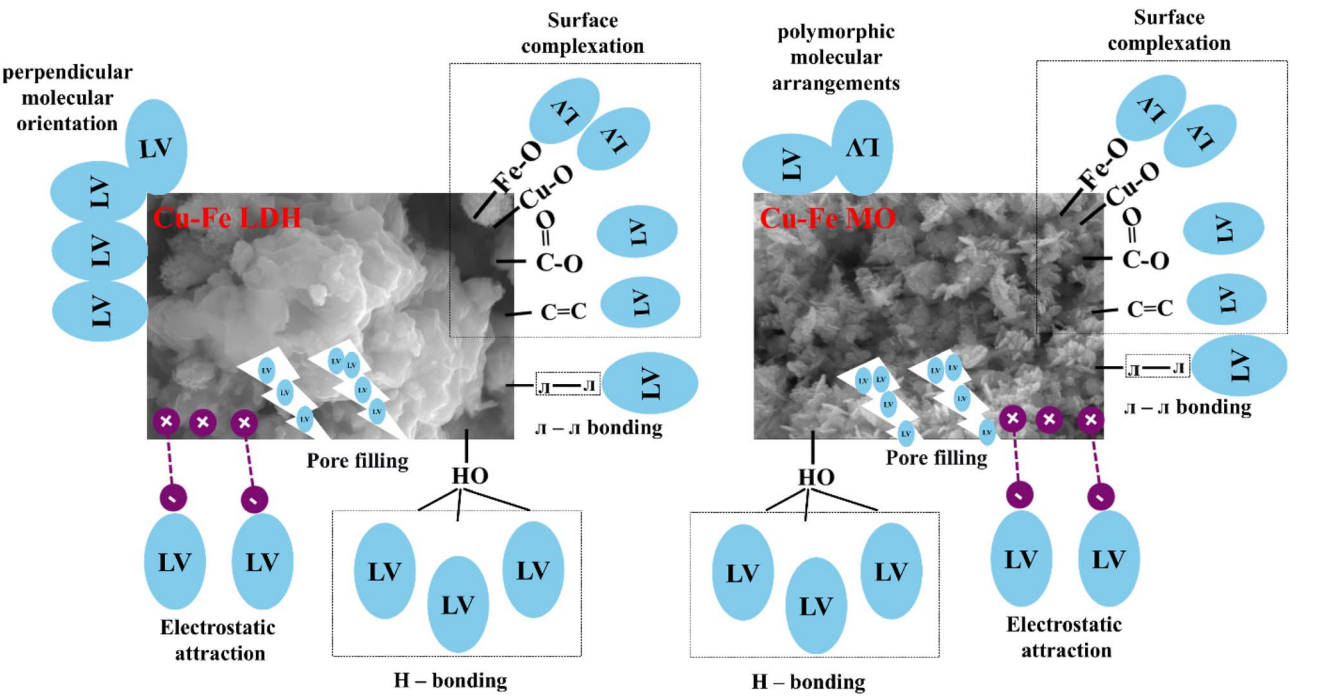

Fig. 11 Proposed adsorption mechanism of LV adsorption onto LDH and MO.

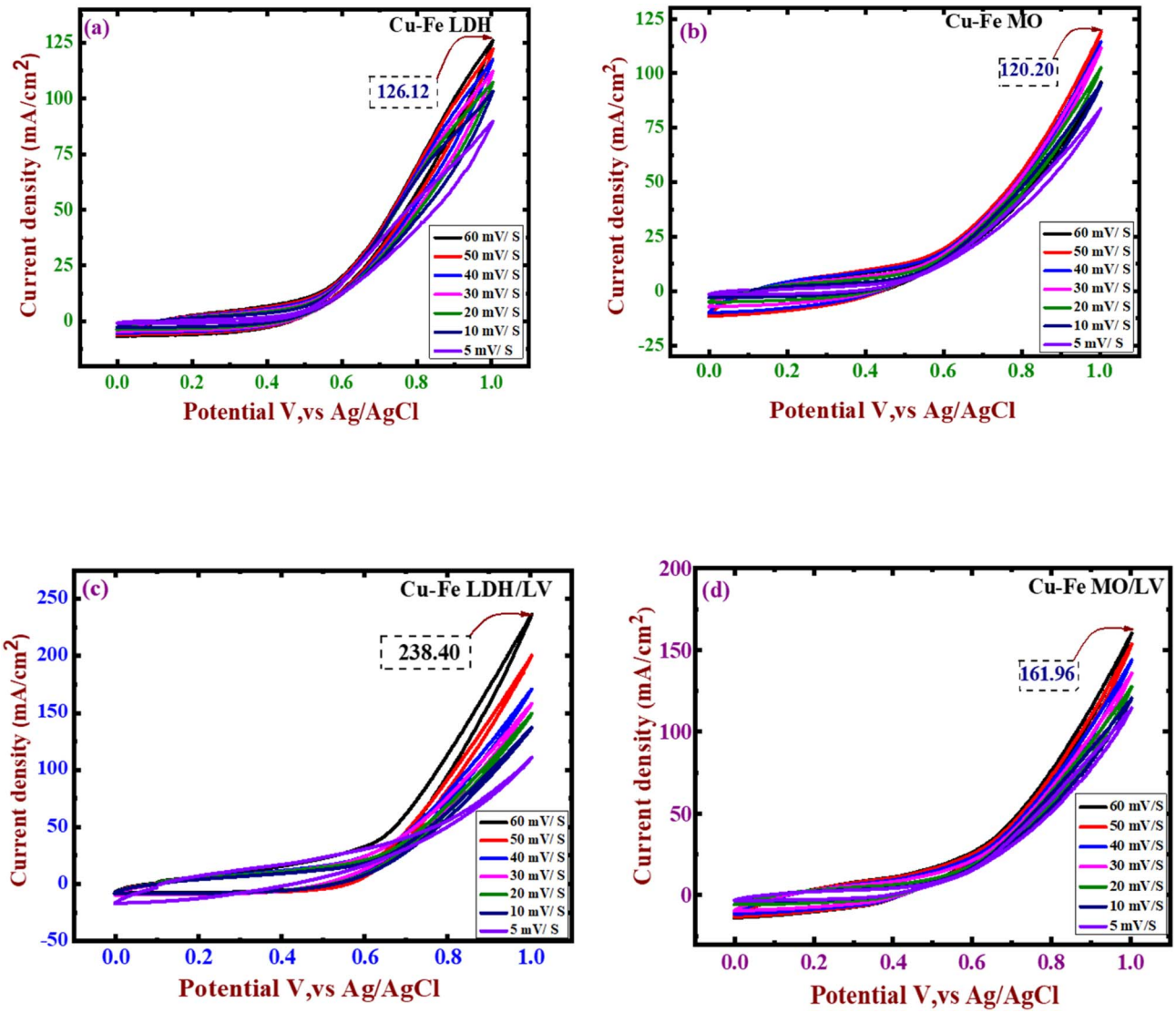

Fig. 12 (CV) curves for (a) Cu–Fe-LDH, (b) MO, (c) LDH/LV and (d) MO/LV.

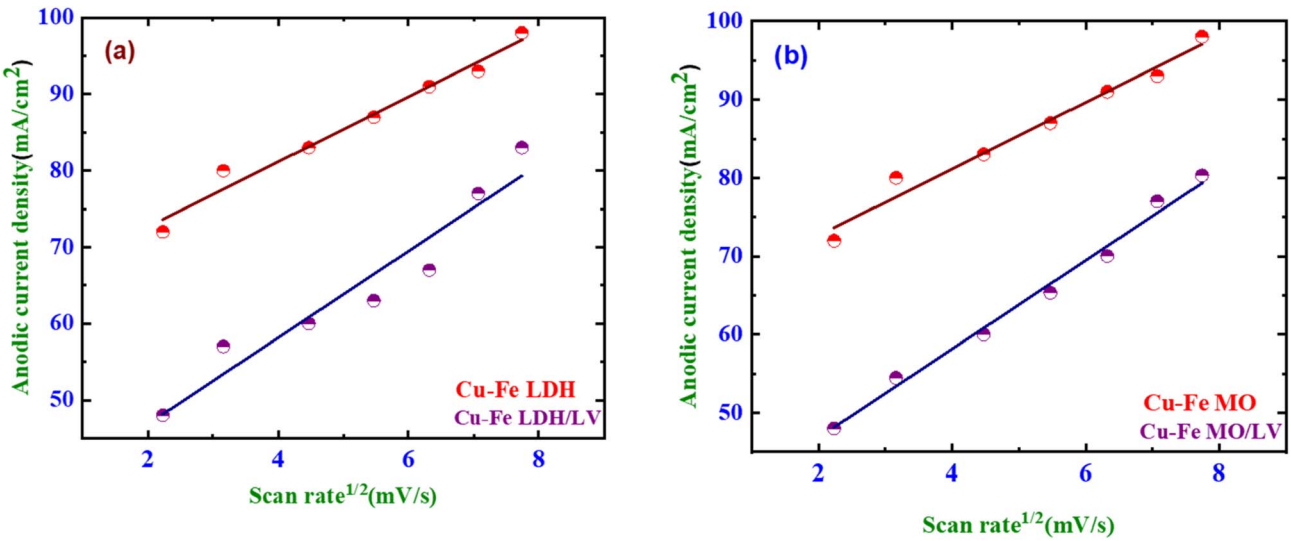

Fig. 13 The relationship between the peak current density and the square root of the scan rates before and after adsorption for (a) LDH before and after adsorption, and (b) MO before and after adsorption.

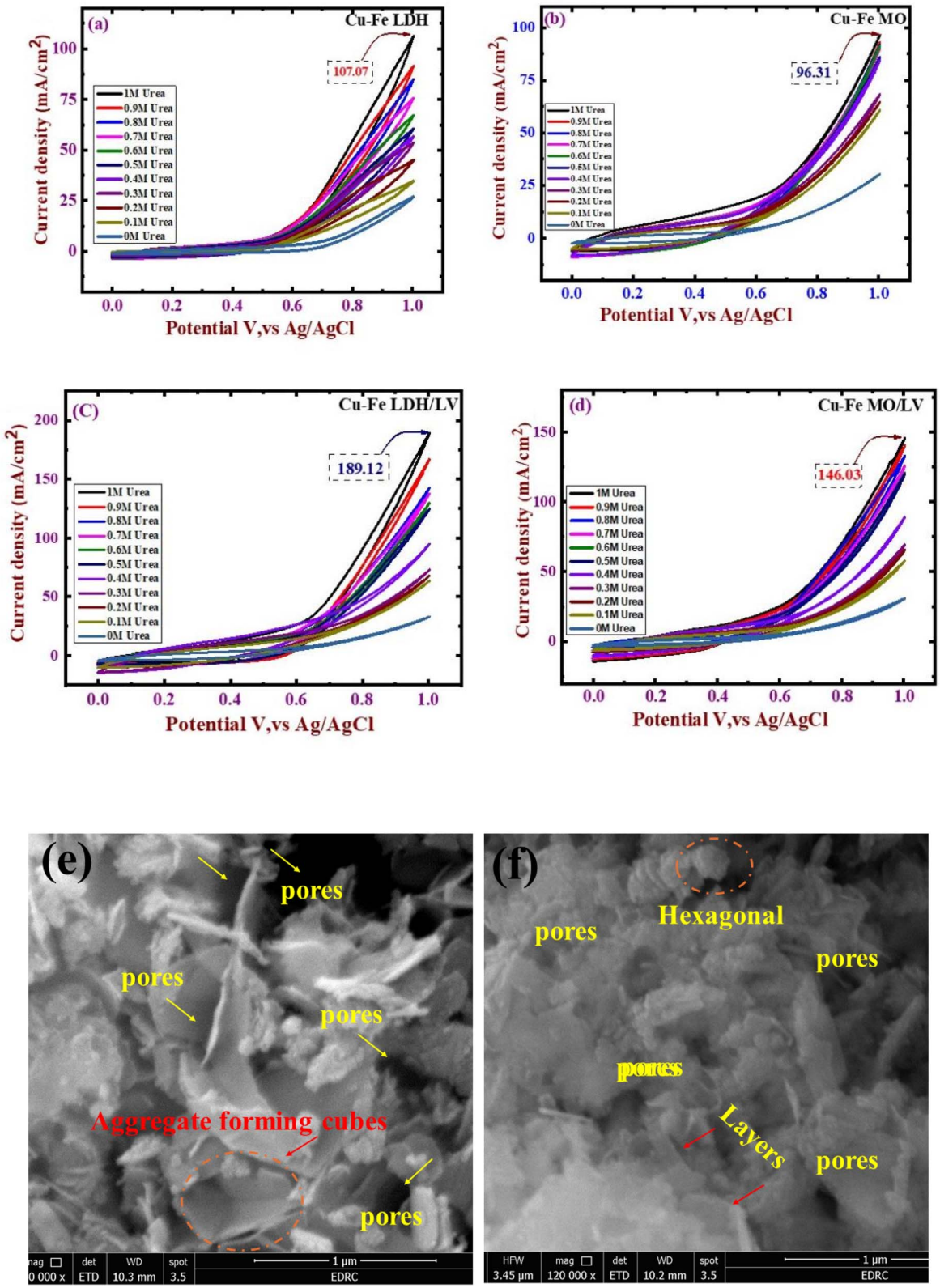

Fig. 14 (CV) curves for (a) Cu–Fe-LDH, (b) Cu–Fe MO, (c) Cu–Fe- LDH/LV, (d) Cu–Fe MO/LV recorded at a concentration ranging from 0 to 1 M within a potential window of 0–1 V and (e–f) SEM images of the Cu–Fe LDH/LV.

and facilitates ion transport, thereby promoting greater accessibility and interaction between the electrode and the adsorbed LV molecules. Additionally, increasing the scan rate leads to an increase in redox reaction rates, as shown in Fig. 13(c), with the electrochemical process being influenced by the diffusion of nitrogen-containing species within the mesoporous structure.

The presence of LV ($C_{18}H_{20}FN_3O_4$), which provides three additional nitrogen-containing functional groups. These groups improve the electrocatalytic efficiency of the electrode material, resulting in increased current density after adsorption.

Fig. 13 shows that at the catalyst's highest electroactivity in 1 M KOH, the plot of current density *versus* the square root of the scan rate is predominantly linear, indicating a diffusion-controlled process. The relationship involving the logarithm of the anodic peak potential further supports this observation. These results suggest that the oxidation process is governed by diffusion mechanisms. With increasing scan rate, the enhancement of oxidation manifests as an increase in the oxidation current density.

3.10.2 Effects of different urea on electrochemical oxidation. The effect of urea concentration on the electrocatalytic activity of four prepared electrode materials was investigated using CV prior to adsorption. As shown in Fig. 14 (a–d), the electrode exhibited a maximum current density of 107.07, 96.31, 189.12 and 146.03 mA cm^{-2} at 1.0 M urea for LDH, MO, LDH/LV and MO/LV, demonstrating superior electrocatalytic performance. This positive correlation indicates that higher urea concentrations enhance the availability of reactant molecules at the electrode/electrolyte interface, thereby facilitating the oxidation reaction.[13,14] The observed improvement in catalytic activity may also result from increased surface accessibility and accelerated electron transfer kinetics at elevated urea levels. These results align with previous studies reporting that increased urea concentration significantly promotes anodic current response due to enhanced mass transport and surface reactivity.[15]

As shown in Fig. 15, the Cu–Fe LDH/LV electrode exhibited a marked increase in current density with rising urea concentration, reaching a maximum of 189.12 mA cm^{-2} at 1.0 M. This represents a substantial enhancement compared to the pre-adsorption value (~107 mA cm^{-2}), indicating that LV adsorption likely promoted surface activation—either by increasing the number of electroactive sites or improving surface conductivity.[16,17]

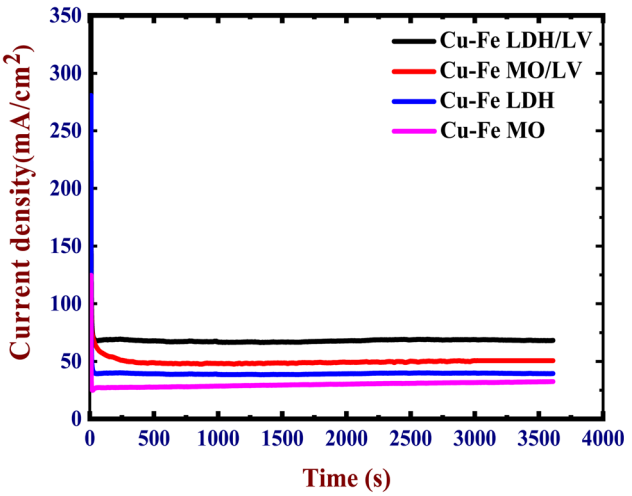

Fig. 15 Chronoamperometric measurements for prepared electrodes through 1 h.

3.10.3 Electrochemical stability. The electrochemical stability of Cu–Fe LDH and Cu–Fe MMO electrodes was evaluated before and after LV adsorption using chronoamperometric current–time measurements. The Cu–Fe LDH/LV electrode demonstrated a consistently high and stable current throughout the measurement period, indicating excellent electrochemical stability following adsorption. This enhanced stability is likely due to improved surface conductivity and effective interaction between LV molecules and the active sites within the LDH structure. The SEM image of the spent adsorbent after LV adsorption reveals that the material retains its layered like morphology, indicating that the structural of the LDH catalyst remains after the adsorption process. No signs of particle collapse, melting, or severe agglomeration are observed, confirming the high structural stability of the material under the experimental conditions.[60] Notably, compared to the LDH before adsorption, the surface appears rougher and partially covered by irregular aggregates, which can be attributed to the adsorption of LV molecules onto the external surface and interlayer regions. The presence of these surface deposits suggests the formation of more pores as shown in the Fig. 14 (e–f) which faceplate the diffusion of urea. As well as, the surface modification is expected to enhance interfacial charge-transfer pathways by introducing nitrogen-containing functional groups and π-conjugated moieties from LV, which can facilitate electron transport during electrochemical measurements.[61]

3.11 The greenness of the proposed method

Assessing the sustainability and environmental friendliness of analytical methodologies is essential for understanding the potential impact of analytical techniques on the environment and ecosystems. The concept of sustainability in analytical chemistry is multifaceted, encompassing aspects such as cost-effectiveness, operational efficiency, safety, waste minimization, and the overall greenness of the procedure MENDELEY CITATION PLACEHOLDER 0. In this work, the sustainability and eco-friendliness of the developed analytical method were systematically evaluated *via* the AGREEprep, BAGI, and RGB12 tools, which provided comprehensive insights into the environmental implications of our approach.[62–64]

The National Environmental Methods Index (NEMI), introduced by the Methods and Data Comparability Board (MDCB) in 2002,[65] is recognized as one of the earliest green analytical chemistry (GAC) assessment tools. The NEMI functions as a searchable database and employs a pictogram divided into four quadrants, each representing a specific environmental criterion. When a criterion is met, the corresponding segment of the pictogram is shaded green, as shown in Fig. 16a.

As a pioneering greenness metric, the NEMI offers several advantages and was effectively utilized in this study to support the development and validation of the proposed method.[66]

AGREEprep was developed as a comprehensive green analytical chemistry (GAC) metric. This tool provides a detailed assessment of the environmental impact of sample preparation procedures,[62] taking into account factors such as the location of sample preparation, safety of solvents used, sustainability of

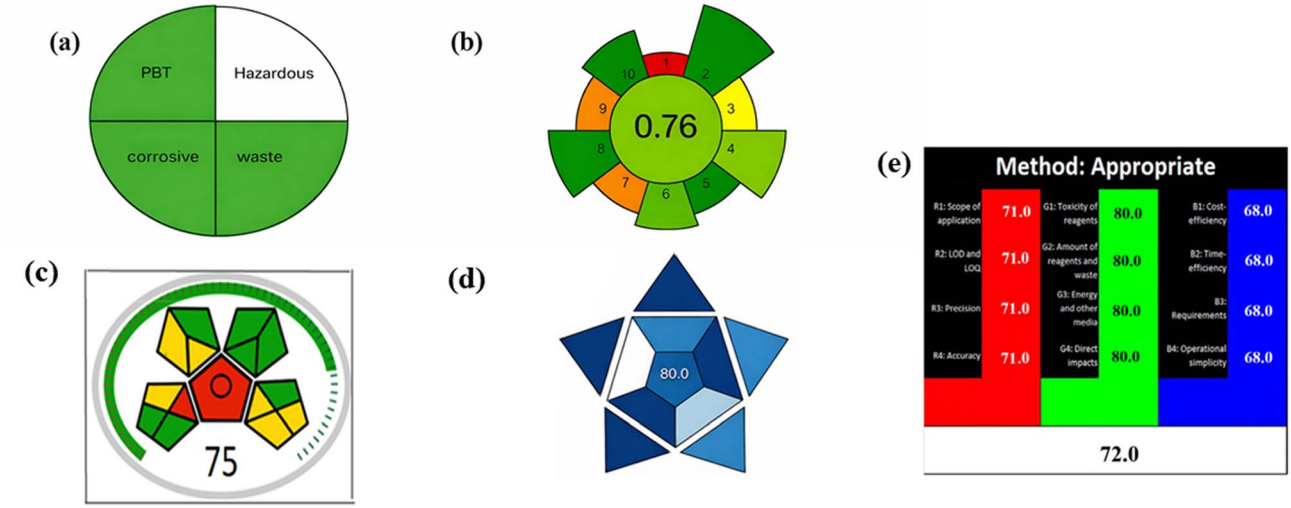

Fig. 16 (a) The NEMI greenness method, (b) the AGREEprep greenness method, (c) the MoGAPI greenness method, (d) BAGI Blueness method, and (e) RGB-12Whiteness method.

materials, minimization of waste, integration and automation of steps, reduction in sample volume, maximization of throughput, reduction in energy consumption, environmentally conscious post preparation configurations, and operator safety. Fig. 16b shows the AGREEprep pictogram.

MoGAPI was the first technique developed for this purpose.[67] The Green Analytical Procedure Index (GAPI) comprises 15 elements that are used to systematically evaluate and quantify the environmental impact of each stage of an analytical procedure, including aspects such as sample preparation, sample volume, health hazards associated with solvents and reagents, instrumentation, waste generation, and waste handling. In the GAPI pictogram, green denotes minimal environmental impact, yellow indicates moderate impact, and red represents significant environmental concerns. The MoGAPI program addresses this by combining the comprehensive overall score calculated *via* the analytical Eco Scale with the visual advantages of the GAPI pictogram[64] (Fig. 16b).

The BAGI tool allows for a quantitative assessment of the "blueness" of a method by considering ten practical criteria. These criteria include evaluation type, total number of analytes, equipment requirements, sample efficiency, sample preparation needs, percentage of analyses, types of reagents and materials used, necessity for preliminary concentration, degree of automation, and sample volume. The composite BAGI index is determined by calculating the approximate mean of the scores for these criteria.[63,64]

In this study, the BAGI tool was applied to assess the blueness of our proposed analytical method. As depicted in Fig. 16d, our method achieved an impressive BAGI score of 80.0, highlighting its outstanding practical applicability, high throughput, strong automation potential, and notably low operational costs.

The RGB12 approach uses 12 distinct algorithms, which are organized into three categories: red, green, and blue; each addresses critical aspects of sustainability. This algorithm integrates the scores from each color group to calculate the overall "whiteness" value, which reflects how well a procedure aligns with the principles of White Analytical Chemistry (WAC). By applying the RGB12 algorithm, a comprehensive quantitative assessment of the overall sustainability of our analytical procedures was performed, allowing for a detailed evaluation of the whiteness profile of the proposed techniques.[64,68]

As illustrated in Fig. 16e, the methods recommended in this study achieved a notable whiteness score of 72.0. This result underscores the improved reliability, performance, and economic viability of our analytical approach.

3.12 Cost analysis

Before the proposed Cu–Fe LDH and Cu–Fe MO composites can be transitioned to large-scale application in water purification, its financial viability must be rigorously established. An analysis of constituent expenses—including precursor materials, energy inputs, and processing chemicals—yields a total manufacturing cost of \$94.2 kg^{-1} for Cu–Fe LDH and \$96.2 kg^{-1} for Cu–Fe MO (Table 7). A market analysis of specialized adsorbents reveals the cost-competitiveness of the Cu–Fe LDH and Cu–Fe MO composite. The synthesis expense for this material is strategically bracketed by two benchmarks: it is substantially more economical than the premium CHI/TiO_2@MWCNT nanohybrid (\$450 kg^{-1}) while commanding a justifiable premium over the low-cost CHI-watermelon rind composite (\$133.50 kg^{-1}). This intermediate cost profile signifies a strategic equilibrium between high adsorption capability and financial practicality. A direct comparison with other LDH-based adsorbents reported in recent literature further contextualizes the production cost (Table 8). It is important to note that literature values are typically reported per gram (USD g^{-1}), whereas the cost in this study is calculated per kilogram (USD kg^{-1}). When converted to consistent units, the synthesis cost for Cu–Fe LDH (~\$0.094 g^{-1}) and Cu–Fe MO (~\$0.096 g^{-1}) is substantially lower than that of many advanced LDH composites, such as Zn–Fe LDH/

Table 7 Total cost involved in preparing 1 kg of Cu–Fe LDH and Cu–Fe MO

Material	Quantity procured	Cumulative procurement cost (in USD)	Procurement expenditure (USD g^{-1} or mL)	Consumed quantity	Expenditure incurred for consumed materials (USD)
$Cu(NO_3)_2$	500 g	35	0.07	100 g	7
$Fe(NO_3)_3$	500 g	17	0.034	50 g	1.7
NaOH	500 g	24.40	0.0488	25 g	1.22
HCL	2.5 L	50	0.02	500 mL	10
Equipment	**Time (H)**	**Max. power (kW)**	**Unit cost of power**	**Cost**	
Stirrer	24	1	0.24	5.76	19.92
Drying	50	1	0.24	12	
Calcination for (MMO)	4	1	0.23	0.92	
Total yield cost of (LDH) 94.2 USD kg^{-1}				Total yield cost of (MMO) 96.4 USD kg^{-1}	

Table 8 Comparative cost analysis of synthesized and literature-reported adsorbents

Material used	Cost (USD g^{-1})	Ref.
Eggshell-modified LDH	8.14	66
Zn–Fe LDH/PANI	12.48	67
LDH adsorbents	19	67
LDH/PU/O-Pom	0.927	68
Cellulose-based Co–Fe LDH	2.55	69
Cu–Fe LDH	0.0942	This study
Cu–Fe MO	0.0964	This study

PANI (\$12.48 g^{-1}) and other benchmark LDH adsorbents (\$8.14–19 g^{-1}).[66,67] While certain studies report lower-cost alternatives utilizing waste biomass (*e.g.*, LDH/PU/O-Pom at ~\$0.93 g^{-1})[68] or simpler chemistries (Cellulose-based Co–Fe LDH at ~\$2.55 g^{-1}).[69] The Cu–Fe composites presented here offer a balanced profile of moderate cost, high adsorption capacity, and additional post-use valorization potential. Therefore, the developed Cu–Fe LDH and Cu–Fe MO composites establish themselves as both economically and ecologically advantageous for sequestering organic contaminants, consistent with sustainable manufacturing protocols. Quantified maximum adsorption capacities of 45.474 mg g^{-1} for the LDH and 59.216 mg g^{-1} for the MO variant attest to their high performance. This pronounced removal efficiency for multiple aquatic pollutants concurrently reinforces the composite's cost-benefit advantage.

4 Conclusion

This study compared the LV adsorption performance of Cu–Fe LDH with its calcined mixed oxide derivative. Analytical characterization confirmed the structural properties of both synthesized composites. Equilibrium and kinetic data for LV removal were accurately modeled by the Langmuir isotherm and pseudo-first-order equation, respectively, with the LDH demonstrating superior uptake capacity. The maximum adsorption capacity for LV was quantified as 45.474 mg g^{-1} (Langmuir q_{max}) on Cu–Fe LDH at 25 °C, increasing to 59.216 mg g^{-1} at 55 °C. In contrast, the Cu–Fe mixed oxide (MO) exhibited lower Langmuir q_{max} capacities of 31.386 mg g^{-1} and 38.68 mg g^{-1} at 25 °C and 55 °C, respectively. Analysis of steric parameters demonstrated that LV adsorption on Cu–Fe LDH proceeds through a multi-molecular mechanism with perpendicular molecular orientation. Conversely, Cu–Fe MO displayed fractional parameter values indicative of polymorphic molecular arrangements at the interface. The formation of additional active sites at higher temperatures further increased the LV uptake capacity for both adsorbents. Thermodynamic analysis revealed a spontaneous adsorption mechanism for LV on both Cu–Fe LDH and Cu–Fe MO. The measured adsorption energies, which increased from below 20 kJ mol^{-1} at 25 °C to values exceeding this threshold at elevated temperatures, signify a transition from an endothermic, physically dominated process to one governed by chemical interactions. Regeneration studies over four consecutive cycles confirmed the materials' sustained efficacy, demonstrating robust reusability. A multi-faceted assessment confirms the viability of the synthesized composites, spanning environmental, functional, and economic dimensions. Quantification through AGREEprep, ESA, and AMVI metrics verified the sustainable nature of the synthesis protocol. Remarkably, the adsorption process augmented the materials' electrocatalytic activity for methanol oxidation; Cu–Fe LDH current density surged from 107 to 189.12 mA cm^{-2}, while Cu–Fe MO increased from ~96 to 146.03 mA cm^{-2}. Economically, production costs were calculated at \$94.2 per kilogram for the LDH variant. Collectively, these findings establish a viable framework for developing cost-effective biosorbents with significant potential for treating wastewater containing cationic antibiotics.

Conflicts of interest

There are no conflicts to declare.

Data availability

The datasets used and/or analyzed during the current study are available from the corresponding author on reasonable request.

Acknowledgements

This work was supported and funded by the Deanship of Scientific Research at Imam Mohammad Ibn Saud Islamic University (IMSIU) (grant number IMSIU-DDRSP2602).

References

1 D. Yang, J. Li, L. Luo, R. Deng, Q. He and Y. Chen, Exceptional levofloxacin removal using biochar-derived porous carbon sheets: Mechanisms and density-functional-theory calculation, *Chem.–Eng. J.*, 2020, **387**, 124103.

2 I. T. Carvalho and L. Santos, Antibiotics in the aquatic environments: a review of the European scenario, *Environ. Int.*, 2016, **94**, 736–757.

3 N. Hanna, P. Sun, Q. Sun, X. Li, X. Yang, X. Ji, H. Zou, J. Ottoson, L. E. Nilsson and B. Berglund, Presence of antibiotic residues in various environmental compartments of Shandong province in eastern China: its potential for resistance development and ecological and human risk, *Environ. Int.*, 2018, **114**, 131–142.

4 F. Meng, Y. Wang, Z. Chen, J. Hu, G. Lu and W. Ma, Synthesis of CQDs@ FeOOH nanoneedles with abundant active edges for efficient electro-catalytic degradation of levofloxacin: Degradation mechanism and toxicity assessment, *Appl. Catal., B*, 2021, **282**, 119597.

5 K. S. Shakhir, F. A. Sulaiman, A. I. Alwared and N. A. Mohammed, Removal of levofloxacin from aqueous solutions by using micro algae: optimization, isotherm, and kinetic study, *Results Eng.*, 2024, **23**, 102529.

6 D. Nasuhoglu, A. Rodayan, D. Berk and V. Yargeau, Removal of the antibiotic levofloxacin (LEVO) in water by ozonation and TiO2 photocatalysis, *Chem. Eng. J.*, 2012, **189**, 41–48.

7 Y. Xiang, Z. Xu, Y. Zhou, Y. Wei, X. Long, Y. He, D. Zhi, J. Yang and L. Luo, A sustainable ferromanganese biochar adsorbent for effective levofloxacin removal from aqueous medium, *Chemosphere*, 2019, **237**, 124464.

8 R. Daghrir and P. Drogui, Tetracycline antibiotics in the environment: a review, *Environ. Chem. Lett.*, 2013, **11**, 209–227.

9 F. M. Mohamed, M. A. Rafea, M. E. A. Zaki, K. A. Alfalous, M. A. Aborziza and M. A. Roshdy, ANOVA and modeling of ciprofloxacin adsorption by MS/EAn@ Cs, *Inorg. Chem. Commun.*, 2025, 115432.

10 R. R. Atta, A. A. Eweis, D. A. Mohammed, A. A. El-Halim, S. A. El-Tawab, M. I. Attallah, M. Bin-Jumah, S. M. Mahgoub and R. Mahmoud, Iron oxide nanoparticles from clove and green coffee for antioxidant and antimicrobial activities and analytical application in caffeine removal, *Sci. Rep.*, 2025, **15**, 35265.

11 A. Elrafey, S. A. Abdel Moaty, E. G. Arafa, O. F. Abdel Gawad, M. M. Kamel, S. A. A. Abdel Aziz, A. A. Allam, H. E. Alfassam and R. Mahmoud, Removal of ciprofloxacin from water: antimicrobial activity and desalination potential using synthetic Ni/Fe clay, *Int. J. Environ. Sci. Technol.*, 2025, 1–28.

12 A. Yazidi, L. Sellaoui, G. L. Dotto, A. Bonilla-Petriciolet, A. C. Fröhlich and A. Ben Lamine, Monolayer and multilayer adsorption of pharmaceuticals on activated carbon: application of advanced statistical physics models, *J. Mol. Liq.*, 2019, **283**, 276–286.

13 X. Guo and J. Wang, A novel monolayer adsorption kinetic model based on adsorbates "infect" adsorbents inspired by epidemiological model, *Water Res.*, 2024, **253**, 121313.

14 D. K. Yadav, S. Uma and R. Nagarajan, Microwave-assisted synthesis of ternary Li-M-Al LDHs (M= Mg, Co, Ni, Cu, Zn, and Cd) and examining their use in phenol oxidation, *Appl. Clay Sci.*, 2022, **228**, 106655.

15 X. Guo, D. Gao, H. He, A. Traitangwong, M. Gong, V. Meeyoo, Z. Peng and C. Li, Promotion of CO2 methanation at low temperature over hydrotalcite-derived catalysts-effect of the tunable metal species and basicity, *Int. J. Hydrogen Energy*, 2021, **46**, 518–530.

16 A. A. Oladipo, A. O. Ifebajo and M. Gazi, Magnetic LDH-based CoO–$NiFe_2O_4$ catalyst with enhanced performance and recyclability for efficient decolorization of azo dye *via* Fenton-like reactions, *Appl. Catal., B*, 2019, **243**, 243–252.

17 P. Gholami, L. Dinpazhoh, A. Khataee, A. Hassani and A. Bhatnagar, Facile hydrothermal synthesis of novel Fe-Cu layered double hydroxide/biochar nanocomposite with enhanced sonocatalytic activity for degradation of cefazolin sodium, *J. Hazard. Mater.*, 2020, **381**, 120742.

18 S.-L. Wang and P.-C. Wang, In situ XRD and ATR-FTIR study on the molecular orientation of interlayer nitrate in Mg/Al-layered double hydroxides in water, *Colloids Surf., A*, 2007, **292**, 131–138.

19 N. de M. C. Serge, R. G. L. Goncalves, K. V. L. Lima, Y. E. S. Correales, J. M. B. T. de Aquino, R. R. Gonçalves, P. Hammer and R. F. P. Nogueira, Consequences of the calcination on the morphological, structural, optical, and catalytic properties of CuMgFe-layered double hydroxide for photo-fenton degradation, *Appl. Clay Sci.*, 2025, **268**, 107740.

20 G. Xu, L. Li, Z. Shen, Z. Tao, Y. Zhang, H. Tian, X. Wei, G. Shen and G. Han, Magnetite Fe3O4 nanoparticles and hematite α-Fe2O3 uniform oblique hexagonal microdisks, drum-like particles and spindles and their magnetic properties, *J. Alloys Compd.*, 2015, **629**, 36–42.

21 S.-B. Lee, E.-H. Ko, J. Y. Park and J.-M. Oh, Mixed metal oxide by calcination of layered double hydroxide: Parameters affecting specific surface area, *Nanomaterials*, 2021, **11**, 1153.

22 A. M. Abdelkawy, F. M. Elantabli, R. Mahmoud, S. M. Mahgoub, F. I. A. El-Ela, H. A. Mohamed and S. A. A. Moaty, Enhanced Zn-Co-Fe Layered Double Hydroxides for Effective Levofloxacin Removal: Innovation in Reuse of Waste Adsorbent, *J. Pharm. Innov.*, 2025, **20**, 86.

23 Z. A. Hammood and A. A. Mohammed, Understanding the sorbent properties of layered double hydroxide for the removal of pharmaceuticals from aqueous Solutions: A comprehensive review, Results, *Chem*, 2025, **13**, 101952.

24 A. A. Toropov, N. Sizochenko, A. P. Toropova and J. Leszczynski, Towards the Development of Global Nano-Quantitative Structure–Property Relationship Models: Zeta Potentials of Metal Oxide Nanoparticles, *Nanomaterials*, 2018, **8**, 243.

25 Z. Rao, K. Li, P. Liu, Y. Lin and X. Lyu, Study on the Thermal Stabilizing Process of Layered Double Hydroxides in PVC Resin, *Molecules*, 2023, **28**, 7792.
26 M. F. Peralta, S. N. Mendieta, I. R. Scolari, G. E. Granero and M. E. Crivello, Synthesis and release behavior of layered double hydroxides–carbamazepine composites, *Sci. Rep.*, 2021, **11**, 20585.
27 I. Z. Awan, P. H. Ho, G. Beltrami, B. Fraisse, T. Cacciaguerra, P. Gaudin, N. Tanchoux, S. Albonetti, A. Martucci, F. Cavani, F. Di Renzo and D. Tichit, Composition Effect on the Formation of Oxide Phases by Thermal Decomposition of CuNiM(III) Layered Double Hydroxides with M(III) = Al, Fe, *Mater.*, 2024, **17**, 83.
28 E. Hussain, M. Jalil, M. Z. Abid, J. Mansab, R. H. Althomali, S. Wang, A. Rauf and K. Rafiq, Materials Advances Insights into the development and performance approach for renewable hydrogen generation, *Mater. Adv.*, 2024, 6572–6585.
29 H. Zhang, J. Li, S. Shu, J. Guo, Y. Liu, W. Cen, X. Li and J. Yang, Catalysts with copper and iron binary metal oxides, *RSC Adv.*, 2022, 35083–35093.
30 A. Chakraborty and H. Acharya, Selective removal of anionic dyes by metal–organic framework-anchored CoAl-layered double hydroxide nanosheets, *ACS Appl. Nano Mater.*, 2021, **4**, 12561–12575.
31 J. Ashtami and P. V Mohanan, Co-precipitation-hydrothermal mediated synthesis, characterization and toxicity evaluation of 2D Zn–Al LDHs in human osteoblast cells, *J. Mater. Sci.*, 2023, **58**, 16809–16821.
32 S. K. Gebreel, A. M. Zayed, M. A. Rafea, N. Mustapha, M. E. A. Zaki, M. A. Roshdy, M. G. Kholief and F. M. Mohamed, Towards zero-wastewaters treatment: biogenic composite for targeted dye congo red adsorption, *Cellulose*, 2025, **32**, 8015–8046.
33 F. M. Mohamed, K. A. Omran, K. A. Alfalous, M. A. Roshdy, S. S. Hassan and H. S. Abu Salem, Attenuation of carcinogenic Cr (VI) using tea waste-anthracite@ Chitosan composite (Tw-An@ Cs) from wastewater; Statistical analysis, *Int. J. Environ. Res.*, 2025, **19**, 203.
34 S. M. Mahgoub, M. R. Shehata, F. L. A. El-ela, A. Farghali, A. Zaher and R. K. Mahmoud, Sustainable waste management and recycling of Zn–Al layered double hydroxide after adsorption of levo fl oxacin as a safe anti-inflammatory, *RSC Adv.*, 2020, 27633–27651.
35 S. Lagergren, About the theory of so-called adsorption of soluble substances, *K. Sven. Vetenskapsakad. Handl.*, 1898, **24**(4), 1–39.
36 Y.-S. Ho and G. McKay, Sorption of dye from aqueous solution by peat, *Chem. Eng. J.*, 1998, **70**, 115–124.
37 O. Alaysuy, M. M. Aljohani, K. Alkhamis, N. M. Alatawi, A. R. Z. Almotairy, K. A. A. Al-Ola, A. S. Khder and N. M. El-Metwaly, Synthesis, characterization and adsorption optimization of bimetallic La–Zn metal organic framework for removal of 2, 4-dichlorophenylacetic acid, *Heliyon*, 2024, **10**(7), e28622.
38 W. J. Weber Jr and J. C. Morris, Kinetics of adsorption on carbon from solution, *J. Sanit. Eng. Div.*, 1963, **89**, 31–59.
39 S. M. Mahgoub, A. S. Alawam, H. A. Rudayni, A. A. Allam, A. M. Radalla, D. A. Tawab and R. Mahmoud, Delafloxacin and Mercury adsorption via a triple-layered metallic hydroxide nanocomposite: Insights into the adsorption mechanism, sustainability, and eco-friendliness studies, *Surf. Interfaces*, 2025, **64**, 106360.
40 A. Mahmoud, F. I. A. El-Ela, R. Mahmoud, A. Z. Shehata, H. Abd El-Raheem, E. Salama, A. A. Allam, H. E. Alfassam and A. Zaher, Eco-friendly moxifloxacin removal using date seed waste and Ni-Fe LDH: Adsorption efficiency and antimicrobial potential, *Ecotoxicol. Environ. Saf.*, 2025, **297**, 118256.
41 A. Naifar, K. Oueslati, F. Aouaini, B. Basha and A. Ben Lamine, Molecular Insights into Crystal Violet Removal Using Natural Clay: A Statistical Physics and PSD/AED Analysis Within the Grand Canonical Ensemble Framework, *Chem. Africa*, 2025, 1–15.
42 A. Naifar, K. Oueslati, E. C. Lima, F. Aouaini and A. Ben Lamine, In-Depth Study of Captopril Adsorption on a Biosourced Adsorbent: Statistical Physics Approach and Pore Characterization, with Modeling of Adsorption Isotherms, Energetic and Steric Analysis, *Langmuir*, 2025, **41**(25), 16115–16127.
43 S. Wjihi, F. Aouaini, A. Erto, M. Balsamo and A. Ben Lamine, Advanced interpretation of CO2 adsorption thermodynamics onto porous solids by statistical physics formalism, *Chem. Eng. J.*, 2021, **406**, 126669.
44 S. Knani, N. Mabrouk, S. T. Alanazi and N. Kechaou, Study of moisture adsorption isotherms characteristics of banana and thermodynamic properties using statistical physics formalism, Dry, *Technol.*, 2022, **40**, 3425–3433.
45 S. I. Yacoub, S. G. Saber, R. A. M. Ali, E. C. Lima, G. S. dos Reis, E. Al-Olayan, Y. F. Salama, M. Mobarak and M. K. Seliem, CTAB-modified alkali-activated binder derived from Favia corals and glass waste: A novel bio-based adsorbent for effective removal of Mn (VII) ions from aqueous solutions, *J. Ind. Eng. Chem.*, 2025, **147**, 406–421.
46 A. S. Elshimy, M. Mobarak, J. S. Ajarem, S. N. Maodaa, A. Bonilla-Petriciolet, Z. Li, M. A. Korany, D. S. Ammar, D. G. Awad and S. A. Elberbash, Sodium alginate-modified alkali-activated eggshell/Fe3O4 nanoparticles: a magnetic bio-based spherical adsorbent for cationic dyes adsorption, *Int. J. Biol. Macromol.*, 2024, **256**, 128528.
47 N. Rahman and A. Raheem, Mechanistic investigation of levofloxacin adsorption on Fe (III)-tartaric acid/xanthan gum/graphene oxide/polyacrylamide hydrogel: box-Behnken design and Taguchi method for optimization, *J. Ind. Eng. Chem.*, 2023, **127**, 110–124.
48 Y. Hu, X. Wei, Y. Hu, W. Wang, J. Fan, X. Liu, W. Chai, Z. Zhou and Z. Ren, Facile preparation of sodium alginate-based gel spheres by droplet polymerization method for removal of levofloxacin from aqueous solution, *Chem. Eng. J.*, 2020, **392**, 123718.
49 S. M. Mahgoub, M. R. Shehata, F. I. A. El-Ela, A. Farghali, A. Zaher and R. K. Mahmoud, Correction: Sustainable waste management and recycling of Zn–Al layered double

hydroxide after adsorption of levofloxacin as a safe anti-inflammatory nanomaterial, *RSC Adv.*, 2020, **10**, 29128.

50 Y. Yu, W. Wang, J. Shi, S. Zhu and Y. Yan, Enhanced levofloxacin removal from water using zirconium (IV) loaded corn bracts, *Environ. Sci. Pollut. Res.*, 2017, **24**, 10685–10694.

51 S. Altaf, R. Zafar, W. Q. Zaman, S. Ahmad, K. Yaqoob, A. Syed, A. J. Khan, M. Bilal and M. Arshad, Removal of levofloxacin from aqueous solution by green synthesized magnetite (Fe3O4) nanoparticles using Moringa olifera: Kinetics and reaction mechanism analysis, *Ecotoxicol. Environ. Saf.*, 2021, **226**, 112826.

52 S. Mpelane, N. Mketo, N. Bingwa and P. N. Nomngongo, Synthesis of mesoporous iron oxide nanoparticles for adsorptive removal of levofloxacin from aqueous solutions: Kinetics, isotherms, thermodynamics and mechanism, *Alexandria Eng. J.*, 2022, **61**, 8457–8468.

53 M. E. Mahmoud, M. F. Amira, M. M. H. M. Azab and A. M. Abdelfattah, Effective removal of levofloxacin drug and Cr(VI) from water by a composed nanobiosorbent of vanadium pentoxide@chitosan@MOFs, *Int. J. Biol. Macromol.*, 2021, **188**, 879–891.

54 M. T. M. H. Hamad and M. E. El-Sesy, Adsorptive removal of levofloxacin and antibiotic resistance genes from hospital wastewater by nano-zero-valent iron and nano-copper using kinetic studies and response surface methodology, *Bioresour. Bioprocess.*, 2023, **10**, 1.

55 J. Li, J. Tao, C. Ma, J. Yang, T. Gu and J. Liu, Carboxylated cellulose nanofiber/montmorillonite nanocomposite for the removal of levofloxacin hydrochloride antibiotic from aqueous solutions, *RSC Adv.*, 2020, **10**, 42038–42053.

56 T. M. Darweesh and M. J. Ahmed, Batch and fixed bed adsorption of levofloxacin on granular activated carbon from date (Phoenix dactylifera L.) stones by KOH chemical activation, *Environ. Toxicol. Pharmacol.*, 2017, **50**, 159–166.

57 F. Pena-Pereira, M. Tobiszewski, W. Wojnowski and E. Psillakis, A tutorial on AGREEprep an analytical greenness metric for sample preparation, *Adv. Sample Prep.*, 2022, **3**, 100025.

58 N. Manousi, W. Wojnowski, J. Płotka-Wasylka and V. Samanidou, Blue applicability grade index (BAGI) and software: a new tool for the evaluation of method practicality, *Green Chem.*, 2023, **25**, 7598–7604.

59 L. Yin, L. Yu, Y. Guo, C. Wang, Y. Ge, X. Zheng, N. Zhang, J. You, Y. Zhang and M. Shi, Green analytical chemistry metrics for evaluating the greenness of analytical procedures, *J. Pharm. Anal.*, 2024, **14**, 101013.

60 Y. Fang, Y. Tang, G. Li, J. Dong, C. Ye, Z. Bu and W. Guo, Synergistic adsorption mechanisms of self-N-doped biochar for levofloxacin elimination: integrated experimental and DFT studies, *Environ. Res.*, 2025, **285**, 122634.

61 J.-M. Liu, Z.-Y. Ji, Y.-B. Shi, P. Yuan, X.-F. Guo, L.-M. Zhao, S.-M. Li, H. Li and J.-S. Yuan, Effective treatment of levofloxacin wastewater by an electro-Fenton process with hydrothermal-activated graphite felt as cathode, *Environ. Pollut.*, 2020, **266**, 115348.

62 F. Pena-Pereira, W. Wojnowski and M. Tobiszewski, AGREE—Analytical GREEnness metric approach and software, *Anal. Chem.*, 2020, **92**, 10076–10082.

63 H. Shaaban, The ecological impact of liquid chromatographic methods reported for bioanalysis of COVID-19 drug, hydroxychloroquine: Insights on greenness assessment, *Microchem. J.*, 2023, **184**, 108145.

64 J. Płotka-Wasylka, A new tool for the evaluation of the analytical procedure: Green Analytical Procedure Index, *Talanta*, 2018, **181**, 204–209.

65 S. El Deeb, K. Abdelsamad and M. K. Parr, Whiter and greener RP-HPLC method for simultaneous determination of dorzolamide, brinzolamide, and timolol using isopropanol as a sustainable organic solvent in the mobile phase, *Separations*, 2024, **11**, 83.

66 A. Elrafey, A. A. Farghali, W. Kamal, A. A. Allam, Z. E. Eldin, H. A. Rudayni, H. E. Alfassam, A. A. A. Anwar, S. Saeed and R. Mahmoud, Cost-effective eggshell-modified LDH composite for caffeine adsorption, cytotoxicity and antimicrobial activity: exploring the synergy and economic viability in search processes, *RSC Adv.*, 2024, **14**, 33281–33300.

67 M. Kamel, G. Abd El-fatah, A. Zaher, A. A. Farghali, S. I. Othman, A. A. Allam, H. A. Rudayni, A. M. Salah, M. E. M. Hassouna and R. Mahmoud, Cost-effective layered double hydroxides/conductive polymer nanocomposites for electrochemical detection of wastewater pollutants, *Chinese J. Anal. Chem.*, 2024, **52**, 100368.

68 R. Abdelazeem, W. Kamal, Z. E. Eldin, M. A. Roshdy, A. A. Allam, S. Saeed, D. A. Tawab, S. I. Othman, A. E. Allah and A. M. Radalla, Exploring the potential of waste biomass of olive as an additive for layered double hydroxide/polyurethane as an effective and safe agent for the adsorption of drug residues: a bioremediation approach, *Mater. Adv.*, 2024, **5**, 9092–9106.

69 A. A. Kotp, A. A. Allam, A. M. Salah, W. Kamal, D. Essam, S. M. Mahgoub, M. A. Mohamed, Z. E. Eldin, H. E. Alfassam, H. A. Rudayni, A. S. Alawam, F. A. Nasr and R. Mahmoud, Cellulose-based CoFe LDH composite as a nano-adsorbent for sulfamethoxazole and cefixime residues: Evaluation of performance, green metrics and cytotoxicity, *J. Contam. Hydrol.*, 2024, **264**, 104364.